Physics-informed regularization and structure preservation for learning stable reduced models from data with operator inference

Nihar Sawant* Boris Kramer[†] Benjamin Peherstorfer*

Abstract

Operator inference learns low-dimensional dynamical-system models with polynomial nonlinear terms from trajectories of high-dimensional physical systems (non-intrusive model reduction). This work focuses on the large class of physical systems that can be well described by models with quadratic and cubic nonlinear terms and proposes a regularizer for operator inference that induces a stability bias onto learned models. The proposed regularizer is physics informed in the sense that it penalizes higher-order terms with large norms and so explicitly leverages the polynomial model form that is given by the underlying physics. This means that the proposed approach judiciously learns from data and physical insights combined, rather than from either data or physics alone. Additionally, a formulation of operator inference is proposed that enforces model constraints for preserving structure such as symmetry and definiteness in linear terms. Numerical results demonstrate that models learned with operator inference and the proposed regularizer and structure preservation are accurate and stable even in cases where using no regularization and Tikhonov regularization leads to models that are unstable.

1 Introduction

With a lack of models and a deluge of data in science and engineering, methods for inferring models from data become ever more important. At the same time, it is increasingly recognized that relying on data alone is insufficient to learn accurate, interpretable, and robust models of science and engineering systems. Instead, a combination of data and physical insights is necessary for learning predictive models [1, 2], which has led to a surge of interest in physics-informed machine learning and scientific machine learning; see, e.g., [3, 4, 5, 6, 7]. In this spirit, we propose a learning method that infers low-dimensional dynamical-system models from data and induces a stability bias via a regularizer that explicitly exploits the polynomial model form given by the underlying physics.

There is a large body of literature on learning dynamical-system models from data. We only review those that are closest to our work. First, there is system identification that originated in the systems and control community [8]. Antoulas and collaborators introduced the Loewner approach [9, 10, 11], which has been extended from linear time-invariant systems to parameterized [12], switched [13], structured [14], delayed [15], bilinear [16], quadratic [17], quadratic bilinear [18], polynomial [19], and parameter-varying [20] systems as well as to learning from time-domain data [21, 22] and noisy data [23, 24, 25]. There is also dynamic mode decomposition (DMD) [26, 27, 28, 29] that best-fits linear operators to state trajectories in the L_2 norm. Methods based on Koopman operators have been developed to extend DMD to nonlinear systems [30, 31, 32]. Finally, there are sparse identification methods such as SINDy [3] and the works [33, 34, 35]. The authors of [36] develop a stability regularizer for SINDy that focuses on quadratic models and is motivated by Lyapunov theory; see also [37]. Similarly, the work [38] adds a loss term to encourage stability of an equilibrium and so learns deep-network models that show stable behavior. Closure modeling is another research direction that recently has seen a surge of interest in data-driven methods [6, 39, 40, 41, 42] and where stabilization plays an important role [43, 44, 45, 46].

^{*}Courant Institute of Mathematical Sciences, New York University

[†]Department of Mechanical and Aerospace Engineering, University of California, San Diego

Our goal is to learn low-dimensional nonlinear dynamical-system models and to penalize unstable models as well as preserve structure and invariances of the dynamical systems from which data are sampled. We build on operator inference [47] that infers reduced models with polynomial nonlinear terms from snapshots data. Operator inference comes with recovery guarantees under certain assumptions [48, 49, 50] and it is a building block of more general learning methods that go far beyond polynomial nonlinear terms and exploit additional physical insights [51, 7, 52, 53, 54, 55, 56, 57]. In [58], operator inference is used together with a physics-informed lifting approach to learn a model of a large-scale combustion system, where it has been shown that regularization is important for obtaining stable models. A Tikhonov regularizer is proposed in [58], which has been further investigated in, e.g., [59, 60]. In contrast, we propose a regularizer that goes beyond Tikohnov regularization and that is explicitly motivated by the nature of the polynomial—in particular, quadratic and cubic polynomials—model form, which in turn is given by the underlying physics. Building on the insights from [61, 62, 63], we penalize quadratic and cubic terms with large norms, which critically and provably influences the stability radius of the learned models and which is also in agreement with the findings in, e.g., [64, 65]. To formulate the corresponding regularizers for operator inference, we derive novel upper bounds for the stability radii of cubic and quadratic-cubic models. We present numerical results that demonstrate improved stability of models learned with the proposed regularization compared to no regularization and Tikhonov regularization. We expect that similar regularization approaches can be used when learning reduced models using different non-intrusive model reduction techniques for the same type of polynomial nonlinear systems.

Section 2 briefly describes learning low-dimensional models with operator inference and motivates this work with a synthetic example. Section 3 proposes the physics-informed regularizer based on new upper bounds of stability radii of polynomial models and structure preservation for operator inference. The computational procedure is discussed in Section 4. Numerical results in Section 5 demonstrate that operator inference with the proposed regularizer learns stable models even when Tikhonov regularization and models learned without regularization are unstable. Concluding remarks are in Section 6.

2 Non-intrusive model reduction with operator inference

Section 2.1 introduces the dynamical systems of interest and Section 2.2 discusses sampling high-dimensional state trajectories. Classical, intrusive model reduction [66, 67, 68, 69] requires the availability of a model of the high-dimensional dynamical system to construct a reduced model and is recapitulated in Section 2.3. In Section 2.4, non-intrusive model reduction with operator inference is summarized, which learns reduced models from state trajectories. The problem formulation and a motivating example are given in Section 2.5.

2.1 Dynamical system with high-dimensional states

Consider a parameterized dynamical system with quadratic and cubic nonlinear terms

$$\frac{\mathrm{d}}{\mathrm{d}t}\boldsymbol{x}(t;\mu) = \boldsymbol{A}(\mu)\boldsymbol{x}(t;\mu) + \boldsymbol{B}(\mu)\boldsymbol{u}(t;\mu) + \boldsymbol{F}(\mu)\boldsymbol{x}(t;\mu)^{2} + \boldsymbol{G}(\mu)\boldsymbol{x}(t;\mu)^{3},$$
(1)

where $\mathbf{A}(\mu) \in \mathbb{R}^{N \times N}$ is the linear operator, and $\mathbf{F}(\mu) \in \mathbb{R}^{N \times N(N+1)/2}$ and $\mathbf{G}(\mu) \in \mathbb{R}^{N \times N(N+1)(N+2)/6}$ are the nonlinear operators. There are $p \in \mathbb{N}$ inputs that enter linearly via the input matrix $\mathbf{B}(\mu) \in \mathbb{R}^{N \times p}$. The system operators depend on a parameter $\mu \in \mathcal{D} \subset \mathbb{R}^d$ that is independent of time. The state dimension is $N \in \mathbb{N}$ and the state at time $t \in [0,T]$ is $\mathbf{x}(t;\mu) \in \mathbb{R}^N$. The p-dimensional input at time t is $\mathbf{u}(t;\mu) \in \mathbb{R}^p$. The initial condition is denoted as $\mathbf{x}_0(\mu) \in \mathbb{R}^N$. To each state $\mathbf{x}(t;\mu) = [x_1(t;\mu), \ldots, x_N(t;\mu)]^T$, we have a corresponding vector $\mathbf{x}(t;\mu)^2 \in \mathbb{R}^{N(N+1)/2}$ defined as

$$\mathbf{x}(t;\mu)^2 = [\mathbf{x}_2^{(1)}(t;\mu)^T, \dots, \mathbf{x}_2^{(N)}(t;\mu)^T]^T$$
 (2)

where $\boldsymbol{x}_2^{(i)}(t;\mu) = x_i(t;\mu)[x_1(t;\mu),\dots,x_i(t;\mu)]^T$ for $i=1,\dots,N$. The vector $\boldsymbol{x}(t;\mu)^2$ contains all pairwise products of components of the state vector $\boldsymbol{x}(t;\mu)$ up to duplicates; see, e.g., [47]. The vector $\boldsymbol{x}(t;\mu)^3 \in$

 $\mathbb{R}^{N(N+1)(N+2)/6}$ is defined as

$$\mathbf{x}(t;\mu)^{3} = [\mathbf{x}_{3}^{(1)}(t;\mu)^{T}, \dots, \mathbf{x}_{3}^{(N)}(t;\mu)^{T}]^{T}$$
(3)

where $\boldsymbol{x}_3^{(i)}(t;\mu) = [x_3^{(i,i)}(t;\mu)^T,\dots,x_3^{(i,N)}(t;\mu)^T]^T$ for $i=1,\dots,N,$ with

$$x_3^{(i,j)}(t;\mu) = x_i(t;\mu)x_j(t;\mu)[x_i(t;\mu),\dots,x_j(t;\mu)]^T$$
 for $j = i,\dots,N$.

2.2 Collecting data

Discretize the time domain into $0 = t_0 < t_1 < \cdots < t_K = T$ and consider the state trajectory

$$\boldsymbol{X}(\mu) = [\boldsymbol{x}_0(\mu), \cdots, \boldsymbol{x}_K(\mu)] \in \mathbb{R}^{N \times K + 1}$$

for a given parameter $\mu \in \mathcal{D}$, initial condition $x_0(\mu)$, and for a given input trajectory

$$U(\mu) = [\boldsymbol{u}(t_1; \mu), \cdots, \boldsymbol{u}(t_K; \mu)] \in \mathbb{R}^{p \times K}$$
.

For example, a trajectory $X(\mu)$ can be obtained by numerically integrating the model (1) of a dynamical system in time. The trajectories

$$m{X}^2(\mu) = [m{x}_0^2(\mu), \cdots, m{x}_K^2(\mu)] \in \mathbb{R}^{N(N+1)/2 \times K+1}$$

 $m{X}^3(\mu) = [m{x}_0^3(\mu), \cdots, m{x}_K^3(\mu)] \in \mathbb{R}^{N(N+1)(N+2)/6 \times K+1}$

can be generated from the state trajectory $X(\mu)$ following definitions (2) and (3), respectively.

2.3 Classical, intrusive model reduction

For each parameter $\mu \in \{\mu_1, \dots, \mu_M\}$ in a set of $M \in \mathbb{N}$ parameters, consider $M_b \in \mathbb{N}$ input trajectories $U_1^b(\mu), \dots, U_{M_b}^b(\mu)$, initial conditions $\boldsymbol{x}_{1,0}^b(\mu), \dots, \boldsymbol{x}_{M_b,0}^b(\mu)$, and the corresponding state trajectories $\boldsymbol{X}_1^b(\mu), \dots, \boldsymbol{X}_{M_b}^b(\mu)$. The state trajectories for all parameters are concatenated into the snapshot matrix

$$\boldsymbol{X}^{b} = [\boldsymbol{X}_{1}^{b}(\mu_{1}), \dots, \boldsymbol{X}_{M_{b}}^{b}(\mu_{1}), \dots, \boldsymbol{X}_{1}^{b}(\mu_{M}), \dots, \boldsymbol{X}_{M_{b}}^{b}(\mu_{M})] \in \mathbb{R}^{N \times KMM_{b}}.$$
(4)

A proper orthogonal decomposition (POD) basis of dimension $n \ll N$ is constructed from the snapshot matrix $\boldsymbol{X}^{\mathrm{b}}$. We do not scale and center the snapshots before applying POD. The basis vectors are the columns of the matrix

$$V = [v_1, \dots, v_n] \in \mathbb{R}^{N \times n}. \tag{5}$$

To construct a projection-based reduced model via Galerkin projection, the reduced operators $\mathbf{A}(\mu) \in \mathbb{R}^{n \times n}$ and $\tilde{\mathbf{B}}(\mu) \in \mathbb{R}^{n \times p}$ are obtained via

$$\tilde{\boldsymbol{A}}(\mu) = \boldsymbol{V}^T \boldsymbol{A}(\mu) \boldsymbol{V}, \qquad \tilde{\boldsymbol{B}} = \boldsymbol{V}^T \boldsymbol{B}(\mu).$$
 (6)

The reduced nonlinear operators $\tilde{F}(\mu) \in \mathbb{R}^{n \times n(n+1)/2}$ and $\tilde{G}(\mu) \in \mathbb{R}^{n \times n(n+1)(n+2)/6}$ are constructed in a similar fashion via projection as described in, e.g., [48]. Thus, for each parameter $\mu \in \{\mu_1, \ldots, \mu_M\}$, one obtains a reduced model

$$\frac{\mathrm{d}}{\mathrm{d}t}\tilde{\boldsymbol{x}}(t,\mu) = \tilde{\boldsymbol{A}}(\mu)\tilde{\boldsymbol{x}}(t;\mu) + \tilde{\boldsymbol{B}}(\mu)\boldsymbol{u}(t;\mu) + \tilde{\boldsymbol{F}}(\mu)\tilde{\boldsymbol{x}}^{2}(t;\mu) + \tilde{\boldsymbol{G}}(\mu)\tilde{\boldsymbol{x}}^{3}(t;\mu),$$
(7)

with reduced state $\tilde{x}(t;\mu) \in \mathbb{R}^n$. We refer to [66, 67, 69] for more details about classical, intrusive model reduction.

2.4 Learning low-dimensional models from data with operator inference

Constructing the reduced operators $\tilde{A}(\mu)$, $\tilde{B}(\mu)$, $\tilde{F}(\mu)$, $\tilde{G}(\mu)$ via (6) is an intrusive process because it requires access to high-dimensional operators $A(\mu)$, $B(\mu)$, $F(\mu)$, $G(\mu)$ in either implicit or explicit form. In contrast, operator inference [47] aims to learn reduced operators from trajectories of dynamical system (1), without requiring access to the high-dimensional operators.

Let V be a basis matrix. Notice that such a basis matrix V can be constructed purely from the snapshot matrix (4) in many situations, without having available the high-dimensional operators. Then, the intrusive projection step (6) is replaced with a non-intrusive least-squares regression problem. First, for each training parameter $\mu \in \{\mu_1, \ldots, \mu_M\}$, consider M_t training input trajectories $U_1(\mu), \ldots, U_{M_t}(\mu)$ with initial conditions $x_{1,0}(\mu), \ldots, x_{M_t,0}(\mu)$ and the corresponding training state trajectories $X_1(\mu), \ldots, X_{M_t}(\mu)$. Second, the training trajectories are projected onto the reduced space via

$$\bar{\boldsymbol{X}}_i(\mu) = \boldsymbol{V}^T \boldsymbol{X}_i(\mu)$$

to obtain the projected training trajectories $\bar{\boldsymbol{X}}_i(\mu) = [\bar{\boldsymbol{x}}_{i,1}(\mu), \dots, \bar{\boldsymbol{x}}_{i,K}(\mu)] \in \mathbb{R}^{n \times K}$ for $i = 1, \dots, M_t$. Third, the operators $\hat{\boldsymbol{A}}(\mu), \hat{\boldsymbol{B}}(\mu), \hat{\boldsymbol{F}}(\mu)$ and $\hat{\boldsymbol{G}}(\mu)$ are fitted via least-squares regression to the projected training trajectories

$$\min_{\hat{\boldsymbol{A}}(\mu),\hat{\boldsymbol{B}}(\mu),\hat{\boldsymbol{F}}(\mu),\hat{\boldsymbol{G}}(\mu)} J(\hat{\boldsymbol{A}}(\mu),\hat{\boldsymbol{B}}(\mu),\hat{\boldsymbol{F}}(\mu),\hat{\boldsymbol{G}}(\mu))$$

with objective function

$$J(\hat{\boldsymbol{A}}(\mu), \hat{\boldsymbol{B}}(\mu), \hat{\boldsymbol{F}}(\mu), \hat{\boldsymbol{G}}(\mu)) = \sum_{i=1}^{M_t} \sum_{k=1}^{K} \left\| \bar{\boldsymbol{x}}'_{i,k}(\mu) - \hat{\boldsymbol{A}}(\mu)\bar{\boldsymbol{x}}_{i,k}(\mu) - \hat{\boldsymbol{B}}(\mu)\boldsymbol{u}_{i,k}(\mu) - \hat{\boldsymbol{F}}(\mu)\bar{\boldsymbol{x}}_{i,k}^2(\mu) - \hat{\boldsymbol{G}}(\mu)\bar{\boldsymbol{x}}_{i,k}^3(\mu) \right\|_{2}^{2},$$
(8)

where $u_{i,k}(\mu)$ is the input at time step k of the ith training trajectory $U_i = [u_{i,1}(\mu), \ldots, u_{i,K}]$ for $i = 1, \ldots, M_t$. The quantity $\bar{x}'_{i,k} \in \mathbb{R}^n$ denotes a numerical approximation of the time derivative of the projected state at time k of the ith trajectory, such as a first-order finite difference approximation

$$\bar{\boldsymbol{x}}_{i,k}' = \frac{\bar{\boldsymbol{x}}_{i,k} - \bar{\boldsymbol{x}}_{i,k-1}}{\delta t}, \tag{9}$$

with time-step size $\delta t > 0$. The inferred operators $\hat{A}(\mu)$, $\hat{B}(\mu)$, $\hat{F}(\mu)$, $\hat{G}(\mu)$ are then used to assemble a low-dimensional model

$$\frac{\mathrm{d}}{\mathrm{d}t}\hat{\boldsymbol{x}}(t;\mu) = \hat{\boldsymbol{A}}(\mu)\hat{\boldsymbol{x}}_k(t;\mu) + \hat{\boldsymbol{B}}(\mu)\boldsymbol{u}_k(\mu) + \hat{\boldsymbol{F}}(\mu)\hat{\boldsymbol{x}}_k^2(t;\mu) + \hat{\boldsymbol{G}}(\mu)\hat{\boldsymbol{x}}_k^3(t;\mu), \tag{10}$$

where $\hat{x}_k(t; \mu) \in \mathbb{R}^n$ is the state at time t.

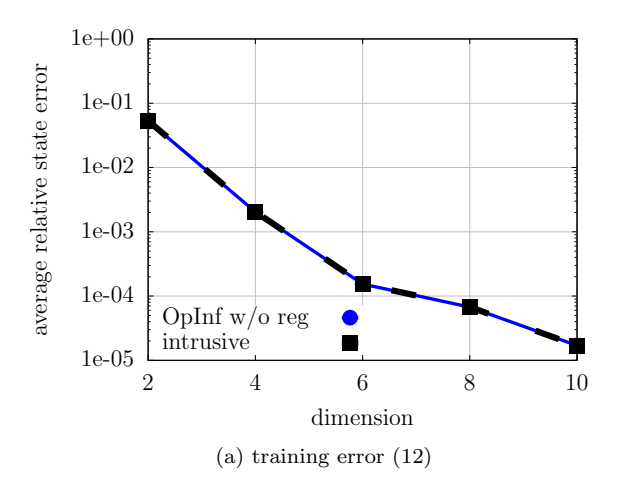
The operator inference process is repeated for each parameter in the training set $\{\mu_1, \ldots, \mu_M\}$ to compute the corresponding inferred operators. For a new parameter $\mu \in \mathcal{D} \setminus \{\mu_1, \ldots, \mu_M\}$, the operators $\hat{A}(\mu), \hat{B}(\mu), \hat{F}(\mu), \hat{G}(\mu)$ are obtained via interpolation. We refer to [47] for details and to [70] for interpolating between reduced operators in model reduction in general.

2.5 Motivating numerical example: Stability of inferred models

We demonstrate operator inference on a toy example. Consider the quadratic dynamical system

$$\frac{\mathrm{d}}{\mathrm{d}t}x(t) = A(\mu)x(t) + Bu(t) + Fx^{2}(t), \qquad (11)$$

where $\boldsymbol{B} \in \mathbb{R}^{N \times 1}$ and $\boldsymbol{F} \in \mathbb{R}^{N \times N(N+1)/2}$ have entries that are realizations of the uniform distribution in [0, 1]. The dimension is N = 128. The linear operator in (11) is $\boldsymbol{A}(\mu) = -\mu(\boldsymbol{A}_s + \boldsymbol{A}_s^T + 2N\boldsymbol{I})$, where \boldsymbol{I} is the identity matrix and $\boldsymbol{A}_s \in \mathbb{R}^{N \times N}$ is a matrix that has as entries realizations of the uniform distribution



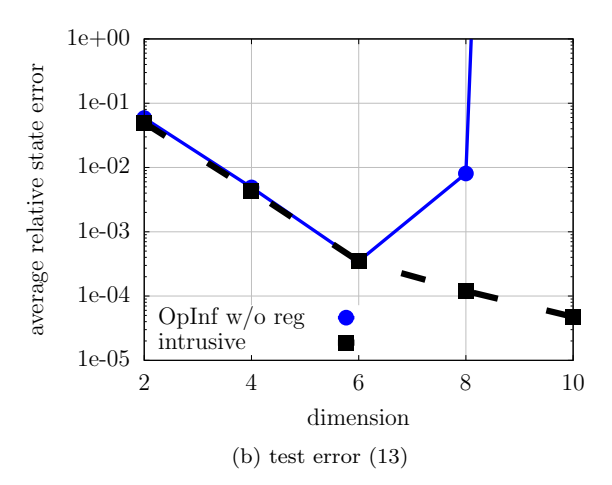


Figure 1: Synthetic example: (a) The training error for the model learned via operator inference (OpInf) matches the error of the model obtained with intrusive model reduction. (b) When tested for a different input and initial condition at the same parameter, the model learned via operator inference (without regularization) is inaccurate and unstable in this example.

in [0,1]. The matrix $\boldsymbol{A}(\mu)$ is symmetric negative definite with probability 1. The parameter domain is $\mathcal{D}=[0.1,1]$ and end time is T=1. We discretize (11) with time-step size $\delta t=10^{-3}$ and explicit Euler. For each training parameter $\mu\in\{0.1,\ldots,1.0\}$, we generate a single $(M_b=1)$ input trajectory $\boldsymbol{U}_1^{\rm b}(\mu)$, whose entries are random with a uniform distribution in [0,2], and an initial condition $\boldsymbol{x}_{1,0}^{\rm b}$, whose entries follow a uniform distribution in [0,1]. The corresponding state trajectories are $\boldsymbol{X}_1^{\rm b}(\mu_1),\ldots,\boldsymbol{X}_1^{\rm b}(\mu_M)$. A basis matrix $\boldsymbol{V}\in\mathbb{R}^{N\times n}$ is then constructed from the corresponding snapshots as described in Section 2.3. The reduced basis is generated for dimension $n=2,\ldots,10$. For parameter $\mu=0.7$, we then construct $M_t=3$ training inputs $\boldsymbol{U}_1,\ldots,\boldsymbol{U}_{M_t}$ with training initial conditions $\boldsymbol{x}_{1,0},\ldots,\boldsymbol{x}_{M_t,0}$, which are sampled from the same distributions as the inputs and initial conditions for the basis construction. The corresponding training state trajectories are $\boldsymbol{X}_1,\ldots,\boldsymbol{X}_{M_t}$, to which we apply operator inference as described in Section 2.4. We use a first-order forward difference scheme to approximate the time derivative as in (9). Additionally, for benchmarking purposes, we also construct a reduced model (7) via the intrusive process described in Section 2.3.

Figure 1a shows the training error of the operator-inference model

$$e_{\text{train}} = \sum_{i=1}^{M_t} \frac{\|\mathbf{V}\hat{\mathbf{X}}_i - \mathbf{X}_i\|_F}{\|\mathbf{X}_i\|_F},$$
 (12)

which indicates that the operator-inference model achieves a comparable error decay as the reduced model obtained from intrusive model reduction. However, if we simulate the operator-inference model at a test input trajectory U^{test} , whose entries are sample uniformly in [0, 10], and test initial condition x_0^{test} , with entries sampled uniformly in [0, 1], and plot the error

$$e_{\text{test}} = \frac{\|\boldsymbol{V}\hat{\boldsymbol{X}}^{\text{test}} - \boldsymbol{X}^{\text{test}}\|_F}{\|\boldsymbol{X}^{\text{test}}\|_F},$$
(13)

in Figure 1b, then an instability can be observed, compared to the reduced model from intrusive model reduction. The results indicate that operator inference is prone to overfitting, which can result in unstable behavior at test inputs as in this motivating example.

3 A physics-informed regularizer for operator inference

We propose a physics-informed regularizer for operator inference that penalizes unstable dynamical-system models. In Sections 3.1-3.3, we recapitulate the definition of the stability radius of quadratic models and derive new bounds for stability radii of cubic and quadratic-cubic dynamical-system models with Lyapunov stability criteria. We then propose a regularizer that penalizes models with small stability radii in Section 3.4. Additionally, in Section 3.5, we propose to combine the physics-informed regularizer with structure preservation. In the following, for each parameter $\mu \in \{\mu_1, \ldots, \mu_M\}$ in the training set, an operator-inference model is learned separately as discussed in Section 2.4. Thus, in this section, the parameter dependence of quantities is not explicitly denoted.

3.1 Stability radius of quadratic models of dynamical systems

We closely follow [63] to define the concept of stability radius for quadratic models of dynamical systems. In fact, the work [63] is the motivation for the proposed physics-informed regularizer.

3.1.1 Stability domain of quadratic models

Consider the autonomous quadratic reduced model

$$\frac{\mathrm{d}}{\mathrm{d}t}\hat{\boldsymbol{x}}(t) = \hat{\boldsymbol{A}}\hat{\boldsymbol{x}}(t) + \hat{\boldsymbol{H}}(\hat{\boldsymbol{x}}(t) \otimes \hat{\boldsymbol{x}}(t))$$
(14)

where \otimes denotes the Kronecker product. Notice that the quadratic term in (14) is denoted with $\hat{\boldsymbol{H}}$ instead of $\hat{\boldsymbol{F}}$ as in the reduced model (7) and the operator-inference model (10). The term $\hat{\boldsymbol{H}}$ is of dimension $n \times n^2$ and acts on the Kronecker product $\hat{\boldsymbol{x}}(t) \otimes \hat{\boldsymbol{x}}(t)$, whereas the quadratic operator $\hat{\boldsymbol{F}}$ is of dimension $n \times n(n+1)/2$ and acts on $\hat{\boldsymbol{x}}^2(t)$ without duplicates due to the commutativity of the multiplication operators, see Section 2.1. However, one can transform between the two different representations. Thus, the model given in (14) is a different representation of an autonomous version of the reduced model (7) and the operator-inference model (10) without a cubic term; cf. Section 3.2. See Section 3.3 for models with cubic terms. Similarly, we can represent a full model with only a quadratic term given in the form of (1) as (14).

Let now without loss of generality $\hat{x}_e = \mathbf{0}$ be an equilibrium point of (14), i.e., $\hat{A}\hat{x}_e + \hat{H}(\hat{x}_e \otimes \hat{x}_e) = \mathbf{0}$. The domain of attraction $\mathcal{A}(\hat{x}_e)$ of the equilibrium \hat{x}_e is then defined as the set of initial conditions that lead to the equilibrium point \hat{x}_e as a steady state, i.e.,

$$\mathcal{A}(\hat{\boldsymbol{x}}_e) = \left\{ \hat{\boldsymbol{x}}_0 : \lim_{t \to \infty} \hat{\boldsymbol{x}}(t) = \hat{\boldsymbol{x}}_e \right\},\$$

where $\hat{x}(t)$ is the state at time t of (14) with initial condition \hat{x}_0 . Directly working with the stability domain is challenging from an analytic and computational point of view and thus one typically resorts to deriving subsets $D \subseteq \mathcal{A}(\hat{x}_e)$. To measure a subset D, we build on the Lyapunov theory to derive a stability radius.

If there exists a Lyapunov function $\nu: \mathbb{R}^N \to \mathbb{R}^+$ that is continuously differentiable and that satisfies

$$\nu(\hat{\boldsymbol{x}}) > 0, \ \dot{\nu}(\hat{\boldsymbol{x}}) < 0, \quad \forall \hat{\boldsymbol{x}} \in \mathcal{A}(\hat{\boldsymbol{x}}_e),$$

then model (14) is locally asymptotically stable about \hat{x}_e . Here, $\dot{\nu}(\hat{x})$ means $\dot{\nu}(\hat{x}) = \frac{\mathrm{d}\nu}{\mathrm{d}\hat{x}}\hat{f}(\hat{x})$, where $\hat{f}(\hat{x}) = \hat{A}\hat{x} + \hat{H}(\hat{x} \otimes \hat{x})$ is the right-hand side function of the corresponding dynamical system. As shown in [61, 62, 63], given a Lyapunov function ν , an estimate $D(\rho) \subseteq \mathcal{A}(\hat{x}_e)$ of the domain of attraction $\mathcal{A}(\hat{x}_e)$ is given by

$$D(\rho) = {\hat{x} : \nu(\hat{x}) \le \rho^2, \ \dot{\nu}(\hat{x}) < 0},$$

where we refer to ρ as the stability radius.

3.1.2 Estimating stability radius

Consider an autonomous quadratic model (14) with Lyapunov function $\nu(\hat{x}) = \hat{x}^T P \hat{x}$, where $P \in \mathbb{R}^{n \times n}$ is a symmetric positive definite matrix that satisfies

$$LL^{T} = -\hat{A}^{T}P - P\hat{A}, \qquad (15)$$

for an arbitrary matrix $L \in \mathbb{R}^{n \times n}$. The derivative of the Lyapunov function along a trajectory is

$$\dot{\nu}(\hat{\boldsymbol{x}}) = \dot{\hat{\boldsymbol{x}}}^T \boldsymbol{P} \hat{\boldsymbol{x}} + \hat{\boldsymbol{x}}^T \boldsymbol{P} \dot{\hat{\boldsymbol{x}}}.$$

Building on [63, Proposition 3.1], we obtain the radius

$$\hat{\rho} = \frac{\sigma_{\min}^2(\mathbf{L})}{2\sqrt{\|\mathbf{P}\|_F}\|\hat{\mathbf{H}}\|_F}$$
(16)

and that $D(\hat{\rho}) \subseteq \mathcal{A}(\hat{x}_e)$ is a subset of $\mathcal{A}(\hat{x}_e)$, if \hat{A} is Hurwitz, i.e., the real parts of all eigenvalues of \hat{A} are negative. Notice that in contrast to the 2-norm $\|\cdot\|_2$ used in [63, Proposition 3.1], we state the radius (16) with respect to the Frobenius norm $\|\cdot\|_F$, which leads to an operator inference problem that can be solved more efficiently than when working with the $\|\cdot\|_2$ norm.

We comment on the bound $\hat{\rho}$ defined in (16) of the stability radius ρ . The same comments apply to the bounds that are derived in the following sections. We will use the bound $\hat{\rho}$ to formulate a regularization term. Thus, what is important for our approach is that penalizing models with a small $\hat{\rho}$ encourages stabler models that have a larger stability radius ρ , and our numerical experiments provide empirical evidence of this. This means that for our approach, it is less critical how close $\hat{\rho}$ is to ρ in absolute terms and more important that $\hat{\rho}$ and ρ follow the same trend in the sense that penalizing a small bound $\hat{\rho}$ leads to a penalization of small ρ .

3.2 Stability radius of cubic models of dynamical systems

Consider the autonomous cubic reduced model

$$\frac{\mathrm{d}}{\mathrm{d}t}\hat{\boldsymbol{x}}(t) = \hat{\boldsymbol{A}}\hat{\boldsymbol{x}}(t) + \hat{\boldsymbol{K}}(\hat{\boldsymbol{x}}(t) \otimes \hat{\boldsymbol{x}}(t) \otimes \hat{\boldsymbol{x}}(t))$$
(17)

which is an equivalent representation of an autonomous version of the reduced model (7) and the operator-inference model (10) with no input and no quadratic term.

Proposition 3.2.1. Let $\nu(\hat{x}) = \hat{x}^T P \hat{x}$ be a Lyapunov function, where $P \in \mathbb{R}^{n \times n}$ is a symmetric positive definite matrix that satisfies (15). Then an estimate of the domain of attraction $\mathcal{A}(\hat{x}_e)$, of the equilibrium point \hat{x}_e of (17), is given by $D(\hat{\rho}) \subseteq \mathcal{A}(\hat{x}_e)$, where

$$\hat{\rho} = \frac{\sigma_{min}(\mathbf{L})}{\sqrt{2\|\hat{\mathbf{K}}\|_F}}.$$
(18)

Proof. A bound of the derivative for the Lyapunov function $\nu(\hat{x})$ along a trajectory is given as

$$\begin{split} \dot{\nu}(\hat{\boldsymbol{x}}) &= \dot{\hat{\boldsymbol{x}}}^T \boldsymbol{P} \hat{\boldsymbol{x}} + \hat{\boldsymbol{x}}^T \boldsymbol{P} \dot{\hat{\boldsymbol{x}}} \\ &= \left[\hat{\boldsymbol{A}} \hat{\boldsymbol{x}} + \hat{\boldsymbol{K}} (\hat{\boldsymbol{x}} \otimes \hat{\boldsymbol{x}} \otimes \hat{\boldsymbol{x}}) \right]^T \boldsymbol{P} \hat{\boldsymbol{x}} + \hat{\boldsymbol{x}}^T \boldsymbol{P} \left[\hat{\boldsymbol{A}} \hat{\boldsymbol{x}} + \hat{\boldsymbol{K}} (\hat{\boldsymbol{x}} \otimes \hat{\boldsymbol{x}} \otimes \hat{\boldsymbol{x}}) \right] \\ &= \hat{\boldsymbol{x}}^T [\hat{\boldsymbol{A}}^T \boldsymbol{P} + \boldsymbol{P} \hat{\boldsymbol{A}}] \hat{\boldsymbol{x}} + (\hat{\boldsymbol{x}} \otimes \hat{\boldsymbol{x}} \otimes \hat{\boldsymbol{x}})^T \hat{\boldsymbol{K}}^T \boldsymbol{P} \hat{\boldsymbol{x}} + \hat{\boldsymbol{x}}^T \boldsymbol{P} \hat{\boldsymbol{K}} (\hat{\boldsymbol{x}} \otimes \hat{\boldsymbol{x}} \otimes \hat{\boldsymbol{x}}) \\ &= -\hat{\boldsymbol{x}}^T \boldsymbol{L} \boldsymbol{L}^T \hat{\boldsymbol{x}} + 2\hat{\boldsymbol{x}}^T \boldsymbol{P} \hat{\boldsymbol{K}} (\hat{\boldsymbol{x}} \otimes \hat{\boldsymbol{x}} \otimes \hat{\boldsymbol{x}}) \\ &\leq -\sigma_{\min}^2(\boldsymbol{L}) \|\hat{\boldsymbol{x}}\|_F^2 + 2\|\hat{\boldsymbol{x}}\|_F^4 \|\boldsymbol{P}\|_F \|\hat{\boldsymbol{K}}\|_F \,. \end{split}$$

We consider the region where the Lyapunov function gradient is negative, which gives us

$$\dot{\nu}(\hat{x}) < 0 \iff \|\hat{x}\|_F^2 < \frac{\sigma_{\min}^2(L)}{2\|P\|_F \|\hat{K}\|_F}.$$

Thus, for the Lyapunov function, the inequality

$$\nu(\hat{\boldsymbol{x}}) = \hat{\boldsymbol{x}}^T \boldsymbol{P} \hat{\boldsymbol{x}} \leq \|\hat{\boldsymbol{x}}\|_F^2 \|\boldsymbol{P}\|_F < \frac{\sigma_{\min}^2(\boldsymbol{L})}{2\|\hat{\boldsymbol{K}}\|_F} = \hat{\rho}^2$$

holds, and thus the stability radius of the cubic system is

$$\hat{\rho} = \frac{\sigma_{\min}(\boldsymbol{L})}{\sqrt{2\|\hat{\boldsymbol{K}}\|_F}} \,.$$

3.3 Stability radius of quadratic-cubic models of dynamical systems

Consider the autonomous quadratic-cubic reduced model

$$\frac{\mathrm{d}}{\mathrm{d}t}\hat{\boldsymbol{x}}(t) = \hat{\boldsymbol{A}}\hat{\boldsymbol{x}}(t) + \hat{\boldsymbol{H}}(\hat{\boldsymbol{x}}(t) \otimes \hat{\boldsymbol{x}}(t)) + \hat{\boldsymbol{K}}(\hat{\boldsymbol{x}}(t) \otimes \hat{\boldsymbol{x}}(t) \otimes \hat{\boldsymbol{x}}(t))$$
(19)

which is a different representation of an autonomous version of the reduced model (7) and the operator-inference model (10).

Proposition 3.3.1. Let $\nu(\hat{x}) = \hat{x}^T P \hat{x}$ be a Lyapunov function, where $P \in \mathbb{R}^{n \times n}$ is a symmetric positive definite matrix that satisfies (15). Then an estimate of the domain of attraction $\mathcal{A}(\hat{x}_e)$, of the equilibrium point \hat{x}_e of (19), is given by $D(\hat{\rho}) \subseteq \mathcal{A}(\hat{x}_e)$, where

$$\hat{\rho} = \frac{\sqrt{\|P\|_F \|\hat{H}\|_F^2 + 2\sigma_{min}^2(L)\|\hat{K}\|_F}}{2\|\hat{K}\|_F} - \frac{\sqrt{\|P\|_F} \|\hat{H}\|_F}{2\|\hat{K}\|_F}.$$
 (20)

Proof. A bound of the derivative of the Lyapunov function along a trajectory is given as

$$\begin{split} \dot{\nu}(\hat{\boldsymbol{x}}) &= \dot{\hat{\boldsymbol{x}}}^T \boldsymbol{P} \hat{\boldsymbol{x}} + \hat{\boldsymbol{x}}^T \boldsymbol{P} \dot{\hat{\boldsymbol{x}}} \\ &= \left[\hat{\boldsymbol{A}} \hat{\boldsymbol{x}} + \hat{\boldsymbol{H}} (\hat{\boldsymbol{x}} \otimes \hat{\boldsymbol{x}}) + \hat{\boldsymbol{K}} (\hat{\boldsymbol{x}} \otimes \hat{\boldsymbol{x}} \otimes \hat{\boldsymbol{x}}) \right]^T \boldsymbol{P} \hat{\boldsymbol{x}} + \hat{\boldsymbol{x}}^T \boldsymbol{P} \left[\hat{\boldsymbol{A}} \hat{\boldsymbol{x}} + \hat{\boldsymbol{H}} (\hat{\boldsymbol{x}} \otimes \hat{\boldsymbol{x}}) + \hat{\boldsymbol{K}} (\hat{\boldsymbol{x}} \otimes \hat{\boldsymbol{x}} \otimes \hat{\boldsymbol{x}}) \right] \\ &= \hat{\boldsymbol{x}}^T [\hat{\boldsymbol{A}}^T \boldsymbol{P} + \boldsymbol{P} \hat{\boldsymbol{A}}] \hat{\boldsymbol{x}} + (\hat{\boldsymbol{x}} \otimes \hat{\boldsymbol{x}})^T \hat{\boldsymbol{H}}^T \boldsymbol{P} \hat{\boldsymbol{x}} + (\hat{\boldsymbol{x}} \otimes \hat{\boldsymbol{x}} \otimes \hat{\boldsymbol{x}})^T \hat{\boldsymbol{K}}^T \boldsymbol{P} \hat{\boldsymbol{x}} + \\ &\hat{\boldsymbol{x}}^T \boldsymbol{P} \hat{\boldsymbol{H}} (\hat{\boldsymbol{x}} \otimes \hat{\boldsymbol{x}}) + \hat{\boldsymbol{x}}^T \boldsymbol{P} \hat{\boldsymbol{K}} (\hat{\boldsymbol{x}} \otimes \hat{\boldsymbol{x}} \otimes \hat{\boldsymbol{x}}) \\ &= -\hat{\boldsymbol{x}}^T \boldsymbol{L} \boldsymbol{L}^T \hat{\boldsymbol{x}} + 2\hat{\boldsymbol{x}}^T \boldsymbol{P} \hat{\boldsymbol{H}} (\hat{\boldsymbol{x}} \otimes \hat{\boldsymbol{x}}) + 2\hat{\boldsymbol{x}}^T \boldsymbol{P} \hat{\boldsymbol{K}} (\hat{\boldsymbol{x}} \otimes \hat{\boldsymbol{x}} \otimes \hat{\boldsymbol{x}}) \\ &\leq -\sigma_{\min}^2(\boldsymbol{L}) \|\hat{\boldsymbol{x}}\|_F^2 + 2\|\hat{\boldsymbol{x}}\|_F^3 \|\boldsymbol{P}\|_F \|\hat{\boldsymbol{H}}\|_F + 2\|\hat{\boldsymbol{x}}\|_F^4 \|\boldsymbol{P}\|_F \|\hat{\boldsymbol{K}}\|_F \,. \end{split}$$

where the matrix L is as defined in (15). We consider the region where the Lyapunov function gradient satisfies $\dot{\nu}(\hat{x}) < 0$, which gives us,

$$-\sigma_{\min}^{2}(\mathbf{L}) + 2\|\hat{\mathbf{x}}\|_{F} \|\mathbf{P}\|_{F} \|\hat{\mathbf{H}}\|_{F} + 2\|\hat{\mathbf{x}}\|_{F}^{2} \|\mathbf{P}\|_{F} \|\hat{\mathbf{K}}\|_{F} < 0.$$
(21)

Roots of the quadratic equation in (21) in $\|\hat{\boldsymbol{x}}\|_F$ are

$$R_{1} = \frac{-\|\boldsymbol{P}\|_{F} \|\hat{\boldsymbol{H}}\|_{F} - \sqrt{\|\boldsymbol{P}\|_{F}^{2} \|\hat{\boldsymbol{H}}\|_{F}^{2} + 2\sigma_{\min}^{2}(\boldsymbol{L})\|\boldsymbol{P}\|_{F} \|\hat{\boldsymbol{K}}\|_{F}}}{2\|\boldsymbol{P}\|_{F} \|\hat{\boldsymbol{K}}\|_{F}}$$

$$R_{2} = \frac{-\|\boldsymbol{P}\|_{F} \|\hat{\boldsymbol{H}}\|_{F} + \sqrt{\|\boldsymbol{P}\|_{F}^{2} \|\hat{\boldsymbol{H}}\|_{F}^{2} + 2\sigma_{\min}^{2}(\boldsymbol{L})\|\boldsymbol{P}\|_{F} \|\hat{\boldsymbol{K}}\|_{F}}}{2\|\boldsymbol{P}\|_{F} \|\hat{\boldsymbol{K}}\|_{F}}$$

Both R_1 and R_2 are non-complex as $\|P\|_F^2 \|\hat{H}\|_F^2 + 2\sigma_{\min}^2(L)\|P\|_F \|\hat{K}\|_F \ge 0$. For \hat{x} with $R_1 < \|\hat{x}\|_F < R_2$, we get

$$(\|\hat{\boldsymbol{x}}\|_{F} - R_{1})(\|\hat{\boldsymbol{x}}\|_{F} - R_{2}) < 0$$

$$\implies -\sigma_{\min}^{2}(\boldsymbol{L}) + 2\|\hat{\boldsymbol{x}}\|_{F}\|\boldsymbol{P}\|_{F}\|\hat{\boldsymbol{H}}\|_{F} + 2\|\hat{\boldsymbol{x}}\|_{F}^{2}\|\boldsymbol{P}\|_{F}\|\hat{\boldsymbol{K}}\|_{F} < 0$$

$$\implies \dot{\nu}(\hat{\boldsymbol{x}}) < 0$$

Because $\|\hat{\boldsymbol{x}}\|_F \geq 0$ and $R_1 \leq 0$, we get,

$$0 \le \|\hat{\boldsymbol{x}}\|_F < R_2$$

as the set of \hat{x} for which the condition $\dot{\nu}(\hat{x}) < 0$ is satisfied. Thus, for the Lyapunov function, the inequality

$$\nu(\hat{x}) = \hat{x}^T P \hat{x} \le \|\hat{x}\|_F^2 \|P\|_F < R_2^2 \|P\|_F = \hat{\rho}^2$$

holds, and thus the stability radius of the quadratic-cubic system is

$$\hat{\rho} = \sqrt{R_2^2 \| \boldsymbol{P} \|_F} = \frac{\sqrt{\| \boldsymbol{P} \|_F \| \hat{\boldsymbol{H}} \|_F^2 + 2\sigma_{\min}^2(\boldsymbol{L}) \| \hat{\boldsymbol{K}} \|_F}}{2 \| \hat{\boldsymbol{K}} \|_F} - \frac{\sqrt{\| \boldsymbol{P} \|_F} \| \hat{\boldsymbol{H}} \|_F}{2 \| \hat{\boldsymbol{K}} \|_F}.$$

3.4 Operator inference with physics-informed regularizer

We now formulate a physics-informed regularizer for learning quadratic, cubic, and quadratic-cubic models with operator inference.

3.4.1 Physics-informed regularizer for quadratic models

For a quadratic nonlinear model, the stability radius $\hat{\rho}$, which is derived in (16), grows inversely proportional to the norm $\|\hat{\boldsymbol{H}}\|_F$ of the quadratic term $\hat{\boldsymbol{H}} \in \mathbb{R}^{n \times n^2}$ in (14). Notice that other results on stability analysis for quadratic systems, e.g., [64, 65], also show that a small norm of the quadratic term can increase the stability radius.

The models that we infer with operator inference have the form (10) and thus the quadratic term \hat{F} is of dimension $n \times n(n+1)/2$. However, models of the form (14) with \hat{H} can be transformed into models with the quadratic operator \hat{F} such that $\hat{F}\hat{x}^2 = \hat{H}(\hat{x}\otimes\hat{x})$ holds for any $\hat{x} \in \mathbb{R}^n$ and $\|\hat{H}\|_F \leq \|\hat{F}\|_F$ holds as well. We can construct \hat{H} such that $\|\hat{H}\|_F = \|\hat{F}\|_F$, by filling the additional columns of \hat{H} with zeros. Thus, we obtain that if we regularize the norm $\|\hat{F}\|_F$, we also regularize the norm $\|\hat{H}\|_F$ of a corresponding \hat{H} , which in turn means that the denominator of the radius $\hat{\rho}$ is regularized. This leads to the optimization problem for inferring model (10) with operator inference and the proposed physics-informed regularizer (PIR-OpInf)

$$\min_{\hat{\boldsymbol{A}},\hat{\boldsymbol{B}},\hat{\boldsymbol{F}}} J(\hat{\boldsymbol{A}},\hat{\boldsymbol{B}},\hat{\boldsymbol{F}},\boldsymbol{0},\lambda) + \lambda \|\hat{\boldsymbol{F}}\|_F^2,$$
(22)

with J defined in (8), with \hat{G} set to the zero matrix because we only infer a quadratic model, and $\lambda > 0$ being a regularization parameter. Notice that increasing λ means more severely penalizing the norm $\|\hat{F}\|_F$, which in turn leads to a potential increase of the radius $\hat{\rho}$ and thus a more stable inferred model in the sense of Lyapunov.

The PIR-OpInf problem (22) imposes no constraints on the linear operator \hat{A} . In particular, there is no guarantee that the inferred \hat{A} is Hurwitz and thus there can exist eigenvalues with non-negative real parts. To ensure a linear operator that is Hurwitz, we apply an eigenvalue reflection as a post-processing step. Let $\hat{A} = Q_A \Sigma_A Q_A^{-1}$ be the eigendecomposition of \hat{A} . If \hat{A} is not diagonalizable, we reduce the dimension n until a matrix \hat{A} is inferred that is diagonalizable. Notice that this process stops in a finite number of

steps because \hat{A} is diagonalizable if n=1 and \hat{A} is non-zero. Without loss of generality, let $\sigma_1, \ldots, \sigma_r$ be eigenvalues with non-negative real parts and let $\sigma_{r+1}, \ldots, \sigma_n$ be all other eigenvalues. Denote with $\mathfrak{R}(\sigma)$ and $\mathfrak{I}(\sigma)$ the real and imaginary part, respectively, for a complex number $\sigma \in \mathbb{C}$. Then, we replace \hat{A} with the matrix

$$Q_A \operatorname{diag}(-\epsilon + \Im(\sigma_1), \dots, -\epsilon + \Im(\sigma_r), \sigma_{r+1}, \dots, \sigma_n) Q_A^{-1}$$

which replaces the positive real parts of the eigenvalues with a negative real number given by the small positive threshold $\epsilon > 0$. Note that the post-processing also needs to be applied after interpolating at a new parameter $\mu \in \mathcal{D}$ outside of the training set; cf. Section 2.4.

In our numerical experiments, when eigenvalues have positive real parts, then they typically have small magnitude because the underlying systems from which data are sampled are stable and thus the instability in the learned model is due to, e.g., insufficient data and other shortcomings of the learning. Because we encounter unstable eigenvalues with small magnitude only, the reflection described in the previous paragraph is sufficient in our experiments. This is in contrast to other settings where the underlying systems are unstable and then eigenvalues of learned system matrices have real parts with large magnitudes. In these cases, other post-processing strategies to obtain Hurwitz linear operators are warranted and we refer to, e.g., [71, 72, 73, 74] for additional details.

3.4.2 Physics-informed regularizer for cubic models

For a cubic nonlinear model, the stability radius $\hat{\rho}$, which is derived in (18), grows inversely proportional to $\|\hat{K}\|_F^{1/2}$ of the cubic term $\hat{K} \in \mathbb{R}^{n \times n^3}$ in (17). The models that we infer with operator inference have the form (10) and thus the cubic term \hat{G} is of dimension $n \times n(n+1)(n+2)/6$. Similar to the quadratic model, (17) with \hat{K} can be transformed into models with cubic operator \hat{G} , such that $\hat{G}\hat{x}^3 = \hat{K}(\hat{x}(t) \otimes \hat{x}(t) \otimes \hat{x}(t))$ holds for any $\hat{x} \in \mathbb{R}^n$ and $\|\hat{K}\|_F \leq \|\hat{G}\|_F$ holds as well. We can construct \hat{K} such that $\|\hat{K}\|_F = \|\hat{G}\|_F$ by filling the additional columns of \hat{K} with zeros. Thus, we obtain that if we regularize the norm $\|\hat{G}\|_F$, we also regularize the norm $\|\hat{K}\|_F$ of a corresponding \hat{K} , which in turn means that the denominator of the radius $\hat{\rho}$ is regularized. For the cubic model, this leads to the optimization problem for inferring model (10) with PIR-OpInf

$$\min_{\hat{\boldsymbol{A}},\hat{\boldsymbol{B}},\hat{\boldsymbol{G}}} J(\hat{\boldsymbol{A}},\hat{\boldsymbol{B}},\boldsymbol{0},\hat{\boldsymbol{G}},\lambda) + \lambda \|\hat{\boldsymbol{G}}\|_F,$$
(23)

with \hat{F} set to the zero matrix because there is no quadratic term. The same post-processing as for quadratic models in Section 3.4.1 is applied to ensure an \hat{A} that is Hurwitz.

3.4.3 Physics-informed regularizer for quadratic-cubic models

For a quadratic-cubic nonlinear model, by taking derivatives of the stability radius $\hat{\rho}$, derived in (20), with respect to $\|\hat{\boldsymbol{H}}\|_F$ and $\|\hat{\boldsymbol{K}}\|_F$ we get,

$$\begin{split} \frac{\partial \hat{\rho}}{\partial \|\hat{\boldsymbol{H}}\|_F} &= \frac{\|\boldsymbol{P}\|_F \|\hat{\boldsymbol{H}}\|_F - \sqrt{\|\boldsymbol{P}\|_F^2 \|\hat{\boldsymbol{H}}\|_F^2 + 2\sigma_{\min}^2(\boldsymbol{L})\|\boldsymbol{P}\|_F \|\hat{\boldsymbol{K}}\|_F}}{2\|\hat{\boldsymbol{K}}\|_F \sqrt{\|\boldsymbol{P}\|_F \|\hat{\boldsymbol{H}}\|_F^2 + 2\sigma_{\min}^2(\boldsymbol{L})\|\hat{\boldsymbol{K}}\|_F}}, \\ \frac{\partial \hat{\rho}}{\partial \|\hat{\boldsymbol{K}}\|_F} &= \frac{\sqrt{\|\boldsymbol{P}\|_F \|\hat{\boldsymbol{H}}\|_F^2} \sqrt{\|\boldsymbol{P}\|_F \|\hat{\boldsymbol{H}}\|_F^2 + 2\sigma_{\min}^2(\boldsymbol{L})\|\hat{\boldsymbol{K}}\|_F} - (\|\boldsymbol{P}\|_F \|\hat{\boldsymbol{H}}\|_F^2 + \sigma_{\min}^2(\boldsymbol{L})\|\hat{\boldsymbol{K}}\|_F)}}{2\|\hat{\boldsymbol{K}}\|_F \sqrt{\|\boldsymbol{P}\|_F \|\hat{\boldsymbol{H}}\|_F^2 + 2\sigma_{\min}^2(\boldsymbol{L})\|\hat{\boldsymbol{K}}\|_F}} \,. \end{split}$$

For $\partial \hat{\rho}/\partial \|\hat{\boldsymbol{H}}\|_F$ we get

$$\begin{split} \|\boldsymbol{P}\|_{F}^{2} \|\hat{\boldsymbol{H}}\|_{F}^{2} + 2\sigma_{\min}^{2}(\boldsymbol{L}) \|\boldsymbol{P}\|_{F} \|\hat{\boldsymbol{K}}\|_{F} &> \|\boldsymbol{P}\|_{F}^{2} \|\hat{\boldsymbol{H}}\|_{F}^{2} \\ \implies \sqrt{\|\boldsymbol{P}\|_{F}^{2} \|\hat{\boldsymbol{H}}\|_{F}^{2} + 2\sigma_{\min}^{2}(\boldsymbol{L}) \|\boldsymbol{P}\|_{F} \|\hat{\boldsymbol{K}}\|_{F}} &> \|\boldsymbol{P}\|_{F} \|\hat{\boldsymbol{H}}\|_{F} \\ \implies \|\boldsymbol{P}\|_{F} \|\hat{\boldsymbol{H}}\|_{F} - \sqrt{\|\boldsymbol{P}\|_{F}^{2} \|\hat{\boldsymbol{H}}\|_{F}^{2} + 2\sigma_{\min}^{2}(\boldsymbol{L}) \|\boldsymbol{P}\|_{F} \|\hat{\boldsymbol{K}}\|_{F}} &< 0 \\ \implies \frac{\partial \hat{\rho}}{\partial \|\hat{\boldsymbol{H}}\|_{F}} &< 0 \,. \end{split}$$

For $\partial \hat{\rho}/\partial \|\hat{K}\|_F$, squaring the two terms in the numerator gives us

$$\left(\sqrt{\|\boldsymbol{P}\|_{F}\|\hat{\boldsymbol{H}}\|_{F}^{2}}\sqrt{\|\boldsymbol{P}\|_{F}\|\hat{\boldsymbol{H}}\|_{F}^{2}+2\sigma_{\min}^{2}(\boldsymbol{L})\|\hat{\boldsymbol{K}}\|_{F}}\right)^{2} = \|\boldsymbol{P}\|_{F}^{2}\|\hat{\boldsymbol{H}}\|_{F}^{4}+2\|\boldsymbol{P}\|_{F}\|\hat{\boldsymbol{H}}\|_{F}^{2}\sigma_{\min}^{2}(\boldsymbol{L})\|\hat{\boldsymbol{K}}\|_{F},$$

$$\left(\|\boldsymbol{P}\|_{F}\|\hat{\boldsymbol{H}}\|_{F}^{2}+\sigma_{\min}^{2}(\boldsymbol{L})\|\hat{\boldsymbol{K}}\|_{F}\right)^{2} = \|\boldsymbol{P}\|_{F}^{2}\|\hat{\boldsymbol{H}}\|_{F}^{4}+2\|\boldsymbol{P}\|_{F}\|\hat{\boldsymbol{H}}\|_{F}^{2}\sigma_{\min}^{2}(\boldsymbol{L})\|\hat{\boldsymbol{K}}\|_{F}+\sigma_{\min}^{4}(\boldsymbol{L})\|\hat{\boldsymbol{K}}\|_{F}^{2}.$$

Comparing the two terms, and using the fact that $\sigma_{\min}^4(L) \|\hat{K}\|_F^2$ and all other terms are non-negative, leads to the inequality

$$\left(\|P\|_{F}\|\hat{H}\|_{F}^{2} + \sigma_{\min}^{2}(L)\|\hat{K}\|_{F}\right)^{2} > \left(\sqrt{\|P\|_{F}\|\hat{H}\|_{F}^{2}}\sqrt{\|P\|_{F}\|\hat{H}\|_{F}^{2} + 2\sigma_{\min}^{2}(L)\|\hat{K}\|_{F}}\right)^{2}$$

$$\Rightarrow \|P\|_{F}\|\hat{H}\|_{F}^{2} + \sigma_{\min}^{2}(L)\|\hat{K}\|_{F} > \sqrt{\|P\|_{F}\|\hat{H}\|_{F}^{2}}\sqrt{\|P\|_{F}\|\hat{H}\|_{F}^{2} + 2\sigma_{\min}^{2}(L)\|\hat{K}\|_{F}}$$

$$\Rightarrow \sqrt{\|P\|_{F}\|\hat{H}\|_{F}^{2}}\sqrt{\|P\|_{F}\|\hat{H}\|_{F}^{2} + 2\sigma_{\min}^{2}(L)\|\hat{K}\|_{F}} - (\|P\|_{F}\|\hat{H}\|_{F}^{2} + \sigma_{\min}^{2}(L)\|\hat{K}\|_{F}) < 0$$

$$\Rightarrow \frac{\partial \hat{\rho}}{\partial \|\hat{K}\|_{F}} < 0.$$

That the partial derivatives are negative, $\partial \hat{\rho}/\partial \|\hat{\boldsymbol{H}}\|_F < 0$ and $\partial \hat{\rho}/\partial \|\hat{\boldsymbol{K}}\|_F < 0$, motivates that decreasing $\|\hat{\boldsymbol{H}}\|_F$ and $\|\hat{\boldsymbol{K}}\|_F$ can increase $\hat{\rho}$, which in turn motivates regularizing with respect to both $\|\hat{\boldsymbol{H}}\|_F$ and $\|\hat{\boldsymbol{K}}\|_F$. As described in Sections 3.4.1 and 3.4.2, by regularizing $\|\hat{\boldsymbol{F}}\|_F$ and $\|\hat{\boldsymbol{G}}\|_F$, we also regularize $\|\hat{\boldsymbol{H}}\|_F$ and $\|\hat{\boldsymbol{K}}\|_F$ respectively. For the quadratic-cubic model, this leads to the optimization problem for inferring model (10) with PIR-OpInf

$$\min_{\hat{A}, \hat{B}, \hat{F}, \hat{G}} J(\hat{A}, \hat{B}, \hat{F}, \hat{G}, \lambda) + \lambda(\|\hat{F}\|_F^2 + \|\hat{G}\|_F).$$
(24)

The same post-processing as for quadratic models in Section 3.4.1 is applied to ensure an \hat{A} that is Hurwitz. A similar approach as described in sections 3.1-3.3 can be used for models with higher order nonlinear terms, to derive the expression for the estimated stability radius and to use it for regularization.

3.5 Operator inference with structure preservation

Structure can be imposed on the linear operator by adding hard constraints to the operator inference problem. We focus on problems that lead to symmetric negative definite linear operators, which are present in, e.g., Hamiltonian systems [54]. We consider the constrained problem

$$\min_{\hat{\boldsymbol{A}},\hat{\boldsymbol{B}},\hat{\boldsymbol{F}},\hat{\boldsymbol{G}}} J(\hat{\boldsymbol{A}},\hat{\boldsymbol{B}},\hat{\boldsymbol{F}},\hat{\boldsymbol{G}}) + \lambda(\|\hat{\boldsymbol{F}}\|_F^2 + \|\hat{\boldsymbol{G}}\|_F),$$
such that $\hat{\boldsymbol{A}} + \epsilon \boldsymbol{I} \leq 0$,

where $\hat{A} + \epsilon I \leq 0$ means that $\hat{A} + \epsilon I$ is symmetric negative semi-definite. The matrix I is the identity and $\epsilon > 0$ is a margin that guarantees that \hat{A} is definite, rather than semi-definite. We refer to (25) as the SPIR-OpInf problem, where the S stands for "structure." Problem (25) is in the class of semi-definite programs, which typically are computationally more expensive to solve than linear least-squares problems as (22) with the same number of unknowns. However, efficient numerical algorithms and software exist for solving semi-definite programs [75]. Additionally, we are seeking low-dimensional models that have few degrees of freedom, which means that we focus mostly on optimization problems with a manageable number of unknowns.

Instead of imposing a margin ϵ to guarantee definiteness of \hat{A} in (25), one can solve problem (25) with the constraint $\hat{A} \leq 0$ and subsequently apply an analogous post-processing step as in Section 3.4. The post-processing described in Section 3.4 preserves symmetry and thus the result is a symmetric negative definite matrix after the post-processing; see also [71]. However, in the following, we will impose a margin ϵ and therefore do not need a post-processing step.

Other structures in the linear operator can be preserved in an analogous way. For example, another common structure is skew-symmetry of \hat{A} which can be formulated as a linear constraint; we leave such other constraints to future work. Recall that it is required to interpolate between inferred operators when a model at a parameter μ outside of the training set is required; cf. Section 2.4. In case of structure-preserving operator inference, the corresponding operator interpolation schemes have to preserve the operator structure. We discuss such an interpolation scheme for symmetric negative definite matrices in Section 4.1.

4 Computational procedure of physics-informed operator inference

In Section 4.1, we briefly recapitulate an interpolation scheme that preserves symmetric definiteness of matrices, which is critical for constructing operators at new parameters outside of the training set in SPIR-OpInf. To select a regularization parameter for PIR-OpInf (22)–(24) and SPIR-OpInf (25), we propose a parameter-selection scheme in Section 4.2 and Section 4.3. Section 4.4 presents Algorithm 1 that summarizes the computational procedure for operator inference with physics-informed regularization and structure preservation.

4.1 Interpolation of structure-preserving operator-inference models

In SPIR-OpInf introduced in Section 3.5, the definiteness and symmetry constraints in the optimization problem (25) ensure that for each training parameter μ_1, \ldots, μ_M a model is obtained with a linear operator that is symmetric negative definite. When we interpolate the trained models at a new parameter $\mu \in \mathcal{D} \setminus \{\mu_1, \ldots, \mu_M\}$ outside of the training set, however, we have to ensure that the interpolated linear operator is symmetric negative definite as well. There are various interpolation schemes in model reduction that preserve such structure, see, e.g., [76, 77]. We build on the Log-Cholesky averaging method presented in [70].

Given are M symmetric negative definite matrices $\hat{\boldsymbol{A}}(\mu_1), \ldots, \hat{\boldsymbol{A}}(\mu_M)$ at parameters μ_1, \ldots, μ_M . We compute the Cholesky factors $\hat{\boldsymbol{L}}(\mu_i)$ such that $\hat{\boldsymbol{A}}(\mu_i) = -\hat{\boldsymbol{L}}(\mu_i)\hat{\boldsymbol{L}}(\mu_i)^T$ for $i = 1, \ldots, M$. The Cholesky factors $\hat{\boldsymbol{L}}(\mu_i)$ are then split into

$$\hat{\boldsymbol{L}}(\mu_i) = \lfloor \hat{\boldsymbol{L}}(\mu_i) \rfloor + \operatorname{diag}(\hat{\boldsymbol{L}}(\mu_i)), \qquad i = 1, \dots, M,$$

where $\operatorname{diag}(\hat{\boldsymbol{L}}(\mu_i))$ is the diagonal matrix with the same the diagonal as $\hat{\boldsymbol{L}}(\mu_i)$ and $\lfloor \hat{\boldsymbol{L}}(\mu_i) \rfloor$ is its remaining strictly lower triangular part. The interpolated matrix $\hat{\boldsymbol{A}}(\mu)$ at a new parameter μ is

$$\hat{\boldsymbol{A}}(\boldsymbol{\mu}) = -\hat{\boldsymbol{L}}(\boldsymbol{\mu})\hat{\boldsymbol{L}}(\boldsymbol{\mu})^T\,,$$

where the Cholesky factor $\hat{\boldsymbol{L}}(\mu)$ is obtained as

$$\hat{\boldsymbol{L}}(\mu) = \mathcal{I}(\mu; \lfloor \hat{\boldsymbol{L}}(\mu_1) \rfloor, \dots, \lfloor \hat{\boldsymbol{L}}(\mu_M) \rfloor) + \exp\left(\mathcal{I}\left(\mu; \log\left(\operatorname{diag}\left(\hat{\boldsymbol{L}}(\mu_1)\right)\right), \dots, \log\left(\operatorname{diag}\left(\hat{\boldsymbol{L}}(\mu_M)\right)\right)\right)\right).$$

The operator \mathcal{I} denotes linear interpolation of the matrix entries at μ and $\exp(\cdot)$ and $\log(\cdot)$ are the matrix exponential and logarithm, respectively.

4.2 A regularization parameter-selection scheme for PIR-OpInf and SPIR-OpInf

Let μ_1, \ldots, μ_M be the training parameters and recall that $\boldsymbol{X}_1(\mu_i), \ldots, \boldsymbol{X}_{M_t}(\mu_i)$ are the training trajectories with input trajectories $\boldsymbol{U}_1(\mu_i), \ldots, \boldsymbol{U}_{M_t}(\mu_i)$, respectively, for $i = 1, \ldots, M$; cf. Section 2.3. Define the minimum λ_{\min} and maximum λ_{\max} of the regularization parameter and discretize the interval $[\lambda_{\min}, \lambda_{\max}] \subset \mathbb{R}$ with m points

$$\lambda_{\min} = \lambda_1 < \dots < \lambda_m = \lambda_{\max}. \tag{26}$$

For each λ_i , we learn a model $\hat{\Sigma}_{ij}$ with PIR-OpInf (22) for μ_j , with $i=1,\ldots,m$ and $j=1,\ldots,M$. In our case, when $\hat{\Sigma}$ refers to a model, then we mean the corresponding matrices that define the model. For example, in the case of a cubic model as in (10), the notation $\hat{\Sigma}$ refers to the matrices $\hat{A}, \hat{B}, \hat{F}$ and \hat{G} , which is different from the way the symbol Σ is typically used in system and control literature where it refers to the system rather than a realization (model) of the system. Then, for $j=2,\ldots,M-1$ and for $i=1,\ldots,m$, we derive $\hat{\Pi}_{ij}$ by interpolating between models

$$\hat{\Sigma}_{i,1}, \dots, \hat{\Sigma}_{i,j-1}, \hat{\Sigma}_{i,j+1}, \dots, \hat{\Sigma}_{i,M}$$
(27)

corresponding to parameters $\mu_1, \ldots, \mu_{j-1}, \mu_{j+1}, \ldots, \mu_M$, i.e., the parameter μ_j corresponding to model $\hat{\Sigma}_{ij}$ is left out from the interpolation process. The interpolation is structure preserving if necessary; cf. Section 4.1. Notice that all models in (27) are trained with the same regularization parameter λ_i . The interpolated model $\hat{\Pi}_{ij}$ is integrated in time with the input trajectories $U_1(\mu_j), \ldots, U_{M_t}(\mu_j)$ corresponding to parameter μ_j to obtain the trajectories $\hat{X}_1^{(i)}(\mu_j), \ldots, \hat{X}_{M_t}^{(i)}(\mu_j)$ and the error

$$e_{ij}^{\text{val}} = \sum_{\ell=1}^{M_t} \frac{\|\boldsymbol{V}\hat{\boldsymbol{X}}_{\ell}^{(i)}(\mu_j) - \boldsymbol{X}_{\ell}(\mu_j)\|_F}{\|\boldsymbol{X}_{\ell}(\mu_j)\|_F}$$
(28)

is assigned to the pair of regularization parameter λ_i and parameter μ_j , where V is the basis matrix. We then pick λ^* by solving

$$\underset{i=1,\dots,m}{\operatorname{arg\,min}} \ \frac{1}{M-2} \sum_{j=2}^{M-1} e_{ij}^{\text{val}}. \tag{29}$$

The same procedure is applied in case of SPIR-OpInf (25).

Notice that error due to interpolating between models enters the validation error (28) and thus the selection criterion (29) for λ^* . This is in contrast to other parameter-selection schemes for operator inference that are either formulated in parameter-independent settings or ignore the parameter dependency in the selection process [58, 59].

4.3 Selecting regularization parameters based on initial conditions

In case the operators are independent of a parameter μ , we select the regularization parameter based on trajectories generated with multiple initial conditions. For initial conditions $\boldsymbol{x}_0^1,\ldots,\boldsymbol{x}_0^{M_t}$, and inputs $\boldsymbol{U}_1,\ldots,\boldsymbol{U}_{M_t}$, the training trajectories are $\boldsymbol{X}_1,\ldots,\boldsymbol{X}_{M_t}$. Define the minimum λ_{\min} and maximum λ_{\max} of the regularization parameter and discretize the interval $[\lambda_{\min},\lambda_{\max}] \subset \mathbb{R}$ with m points

$$\lambda_{\min} = \lambda_1 < \dots < \lambda_m = \lambda_{\max}.$$

Algorithm 1: Operator inference with physics-informed regularizer and structure preservation

Input: basis V, inputs $U_1(\mu_j), \dots, U_{M_t}(\mu_j)$ and trajectories $X_1(\mu_j), \dots, X_{M_t}(\mu_j)$ for $j=1,\dots,M$ Output: inferred operators $\hat{A}(\mu_j), \hat{B}(\mu_j), \hat{F}(\mu_j), \hat{G}(\mu_j)$ for $j=1,\dots,M$ 1 for $i=1,\dots,m$ do

2 for $j=1,\dots,M$ do

3 Infer operators $\hat{A}^{(i)}(\mu_j), \hat{B}^{(i)}(\mu_j), \hat{F}^{(i)}(\mu_j), \hat{G}^{(i)}(\mu_j)$ with either PIR-OpInf (22) or SPIR-OpInf (25) and regularization parameter λ_i defined in (26) and training parameter μ_j 4 Compute validation error (28) for $i=1,\dots,m$ and $j=2,\dots,M-1$ 5 Pick $\lambda^* = \lambda_{i^*}$ with index i^* as in (29) that minimizes validation error

6 Set $\hat{A}(\mu_j) = \hat{A}^{(i^*)}(\mu_j), \hat{B}(\mu_j) = \hat{B}^{(i^*)}(\mu_j), \hat{F}(\mu_j) = \hat{F}^{(i^*)}(\mu_j), \hat{G}(\mu_j) = \hat{G}^{(i^*)}(\mu_j)$ for $j=1,\dots,M$

We split the training data into L different folds, with the data in each fold being

7 return $\hat{A}(\mu_1), \dots, \hat{A}(\mu_M), \hat{B}(\mu_1), \dots, \hat{B}(\mu_M), \hat{F}(\mu_1), \dots, \hat{F}(\mu_M), \hat{G}(\mu_1), \dots, \hat{G}(\mu_M)$

$$\mathbf{X}_{l}^{f} = \begin{cases} [\mathbf{X}_{(l-1)f_{l}+1} \dots \mathbf{X}_{lf_{l}}], & \text{for } l = 1, \dots, L-1 \\ [\mathbf{X}_{(l-1)f_{l}+1} \dots \mathbf{X}_{M_{t}}], & \text{for } l = L \end{cases}$$
(30)

with the rounded value $f_l = \left\lfloor \frac{M_t}{L} \right\rfloor$. For fold l, define the validation data as

$$\bar{\boldsymbol{X}}_{l}^{f} = \begin{cases} [\boldsymbol{X}_{f_{l}+1} \dots \boldsymbol{X}_{M_{t}}], & \text{for } l = 1\\ [\boldsymbol{X}_{1} \dots \boldsymbol{X}_{(l-1)f_{l}} \boldsymbol{X}_{lf_{l}+1} \dots \boldsymbol{X}_{M_{t}}], & \text{for } l = 2, \dots, L-1\\ [\boldsymbol{X}_{1} \dots \boldsymbol{X}_{(l-1)f_{l}}], & \text{for } l = L. \end{cases}$$

For each λ_i , we learn the model $\hat{\Sigma}_{il}$ with PIR-OpInf (22), using the data $\bar{\boldsymbol{X}}_l^f$, with $i=1,\ldots,m$ and $l=1,\ldots,L$. The learned model $\hat{\Sigma}_{il}$ is integrated in time with input trajectories and initial conditions corresponding to \boldsymbol{X}_l^f , to obtain trajectories $\hat{\boldsymbol{X}}_l^f(\lambda_i)$, and the error

$$e_{il}^{\text{val}} = \frac{\|\boldsymbol{V}\hat{\boldsymbol{X}}_{l}^{f}(\lambda_{i}) - \boldsymbol{X}_{l}^{f}\|_{F}}{\|\boldsymbol{X}_{l}^{f}\|_{F}}$$
(31)

is assigned to the pair of regularization parameter λ_i and fold l, where V is the basis matrix. We then pick λ^* by solving

$$\underset{i=1,...,m}{\operatorname{arg\,min}} \ \frac{1}{L} \sum_{l=1}^{L} e_{il}^{\text{val}}. \tag{32}$$

4.4 Algorithm of operator inference with physics-informed regularizer and structure preservation

Algorithm 1 summarizes the computational procedure of the proposed approach. Inputs are the basis matrix V, which is constructed from trajectories as described in Section 2.3, and the training trajectories $X_1(\mu_i), \ldots, X_{M_t}(\mu_i)$ and inputs $U_1(\mu_i), \ldots, U_{M_t}(\mu_i)$ for the training parameter μ_i with $i = 1, \ldots, M$. In the nested for loop, models are generated with either PIR-OpInf (22) or SPIR-OpInf (25) for all pairwise combinations of regularization parameters defined in (26) and training parameters μ_1, \ldots, μ_M . Then, the validation error (28) is computed and the index i^* of the regularization parameter λ_{i^*} that minimizes the validation error is determined. The corresponding inferred models are returned.

5 Numerical experiments

In this section, we compare operator inference with the proposed physics-informed regularizer (PIR-OpInf) and structure preservation (SPIR-OpInf) to Tikhonov regularization and operator inference without regularization. Section 5.1 revisits the synthetic example from Section 2.5. Sections 5.2–5.5 show experiments with the Burgers' equation, a reaction-diffusion problem in a pipe, phase separation described by an Allen-Cahn model, and a FitzHugh-Nagumo model. The proposed approach depends on a small, positive threshold $\epsilon > 0$, e.g., for the post-processing in PIR-OpInf (cf. Section 3.4) and for the margin in SPIR-OpInf (25), which we set to $\epsilon = 10^{-10}$ in all of the following experiments.

5.1 Synthetic example

Consider again the synthetic example introduced in Section 2.5. We now apply PIR-OpInf with the parameter selection procedure discussed in Section 4.2. For each dimension $n \in \{2,4,6,8,10\}$, we sweep over m=51 regularization parameters that are log-uniformly distributed in the interval $[10^{-15}, 10^5]$. The selected regularization parameters are $\lambda^* = 10^{-10}, 1.58 \times 10^{-7}, 10^{-8}, 3.98 \times 10^{-9}, 1.58 \times 10^{-9}$ for dimensions n=2,4,6,8,10, respectively. We choose the test parameter set $\{\mu_1^{\text{test}},\ldots,\mu_{M_{\text{test}}}^{\text{test}}\}$ of $M_{\text{test}}=7$ test parameters that are equidistantly chosen in \mathcal{D} , where for each test parameter a test input trajectory is constructed with entries sampled uniformly in [0,10] and a test initial condition with entries sampled uniformly in [0,1], cf. Section 2.5.

Figure 2a shows the test error

$$e_{\text{test}} = \sum_{i=1}^{M_{\text{test}}} \frac{\|\boldsymbol{V}\bar{\boldsymbol{X}}^{\text{test}}(\boldsymbol{\mu}_{i}^{\text{test}}) - \boldsymbol{X}^{\text{test}}(\boldsymbol{\mu}_{i}^{\text{test}})\|_{F}}{\|\boldsymbol{X}^{\text{test}}(\boldsymbol{\mu}_{i}^{\text{test}})\|_{F}},$$
(33)

where $\bar{X}^{\text{test}}(\mu_i^{\text{test}})$ is the trajectory obtained at test parameter μ_i^{test} with the corresponding test input trajectory and test initial condition with either PIR-OpInf, OpInf without regularization, or intrusive model reduction. In contrast to OpInf without regularization, PIR-OpInf shows stable behavior and yields accurate predictions even for dimensions n>6 in this example. Figure 2b shows the stability radius $\hat{\rho}$ defined in (16) for PIR-OpInf, OpInf without regularization, and intrusive model reduction. To compute the bound (16) of the stability radius, we draw matrices \boldsymbol{L} with entries uniformly distributed in [0, 1] and repeat the calculation 100 times. We then show the median and the 25% and 75% quantile in Figure 2b. The median of the stability radius of the model obtained with PIR-OpInf is larger than the median of the stability radius of OpInf without regularization, which numerically demonstrates that the proposed physics-informed regularizer indeed induces a stability bias.

5.2 Burgers' equation

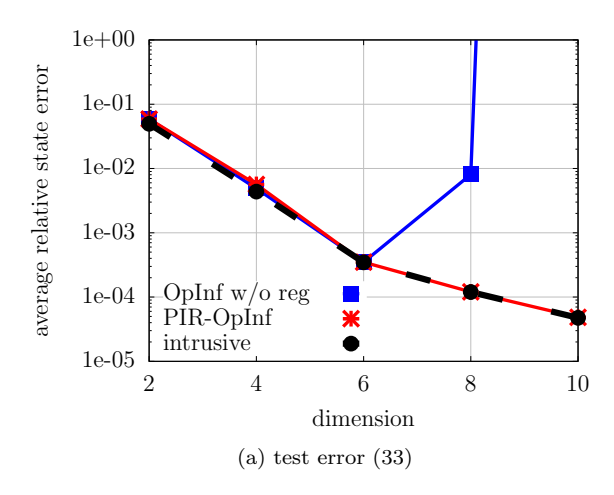
We consider the parameterized Burgers' equation

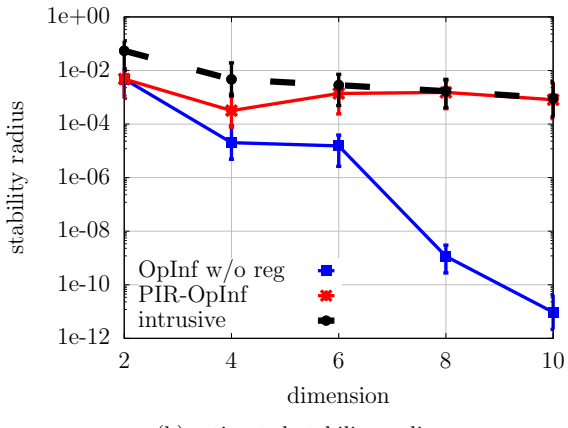
$$\frac{\partial x}{\partial t}(\omega, t; \mu) = \mu \frac{\partial^2 x}{\partial^2 \omega}(\omega, t; \mu) - x(\omega, t; \mu) \frac{\partial x}{\partial \omega}(\omega, t; \mu)$$

with spatial coordinate $\omega \in (0,1)$, time $t \in [0,1]$, and viscosity $\mu \in [10,100]$. Dirichlet boundary conditions $x(0,t;\mu) = u(t), \ x(1,t;\mu) = 0$ are imposed, with input $u : [0,1] \to \mathbb{R}$. The equation is discretized in space with finite differences on an equidistant grid in [0,1] with N = 128 grid points. Time is discretized with the explicit Euler method with time-step size $\delta t = 10^{-4}$.

5.2.1 Problem setup

For each of the M=10 training parameters $\mu=\{10,20,30,\ldots,100\}$, we derive a single input trajectory $U_1^{\rm b}(\mu)$, with entries uniformly sampled in [0,2], and an initial condition $\boldsymbol{x}_1(\mu)=\boldsymbol{0}$. Thus, $M_b=1$. The corresponding state trajectories are $\boldsymbol{X}_1^{\rm b}(\mu_1),\ldots,\boldsymbol{X}_1^{\rm b}(\mu_M)$. A basis matrix $\boldsymbol{V}\in\mathbb{R}^{N\times n}$ is then constructed





(b) estimated stability radius

Figure 2: Synthetic example: The model obtained with the proposed PIR-OpInf shows stable behavior, in contrast to OpInf without regularization, and achieves a comparable test error as intrusive model reduction. The estimated stability radius (16) of the PIR-OpInf model is orders of magnitude larger than the estimated stability radius of the OpInf model without regularization, which is in agreement with the aim of the proposed regularizer to penalize models with low stability radii.

from the corresponding snapshots as described in Section 2.3. Furthermore, we sample $M_t = 10$ training inputs $U_1(\mu), \ldots, U_{M_t}(\mu)$ for each training parameter $\mu \in \{10, \ldots, 100\}$. To generate the initial conditions $x_{1,0}(\mu), \ldots, x_{M_t,0}(\mu)$ for each training parameter $\mu \in \{10, \ldots, 100\}$, we sample *n*-dimensional random vectors $r_1(\mu), \ldots, r_{M_t}(\mu)$ with independent entries uniformly distributed in [0,1] and set $x_{i,0}(\mu) = Vr_i(\mu)$ for $i = 1, \ldots, M_t$. We apply parameter selection as in Section 4.2 to find regularization parameters for each dimension $n \in \{2, \ldots, 10\}$. Furthermore, we construct an operator-inference model obtained without regularization and a reduced model with intrusive model reduction.

For comparison purposes, we also construct from the same training data an operator-inference model with the regularization proposed in [59, 58], which is Tikhonov regularization that regularizes the Frobenius norms of linear, quadratic, and input operators together, rather than only the norm of the quadratic operator as in the proposed PIR-OpInf. We refer to this approach as T-OpInf in the following. The same regularization parameter-selection procedure is applied as for PIR-OpInf.

5.2.2 Results for PIR-OpInf

We test the models at $M_{\text{test}} = 7$ test parameters that are equidistantly distributed in the parameter domain \mathcal{D} . For each test parameter $\mu \in \{\mu_1^{\text{test}}, \dots, \mu_{M_{\text{test}}}^{\text{test}}\}$, we generate $M'_{\text{test}} = 5$ input trajectories $U_1^{\text{test}}(\mu), \dots, U_{M'_{\text{test}}}^{\text{test}}(\mu)$ and the corresponding test state trajectories $X_1^{\text{test}}(\mu), \dots, X_{M'_{\text{test}}}^{\text{test}}(\mu)$. The test initial conditions are the same as the training initial conditions, i.e, $x_{i,0}^{\text{test}}(\mu) = x_{i,0}(\mu)$, for $i = 1, \dots, M'_{\text{test}}$. The test error is then given by

$$e_{\text{test}} = \sum_{i=1}^{M_{\text{test}}} \sum_{i=1}^{M'_{\text{test}}} \frac{\| V \bar{X}_{j}^{\text{test}}(\mu_{i}^{\text{test}}) - X_{j}^{\text{test}}(\mu_{i}^{\text{test}}) \|_{F}}{\| X_{j}^{\text{test}}(\mu_{i}^{\text{test}}) \|_{F}},$$
(34)

where the trajectories $\bar{\boldsymbol{X}}_{j}^{\text{test}}(\mu_{i}^{\text{test}})$ for $i=1,\ldots,M_{\text{test}}$ and $j=1,\ldots,M'_{\text{test}}$ are obtained from either operator inference without regularization, PIR-OpInf, or intrusive model reduction.

Figure 3a, Figure 3c, and Figure 3e show the test error (34) for test inputs with entries sampled uniform from the domains [0, 2], [0, 3], and [0, 4], respectively. In all cases, PIR-OpInf shows stable behavior, whereas OpInf without regularization leads to numerical instabilities. Even T-OpInf with Tikhonov regularization

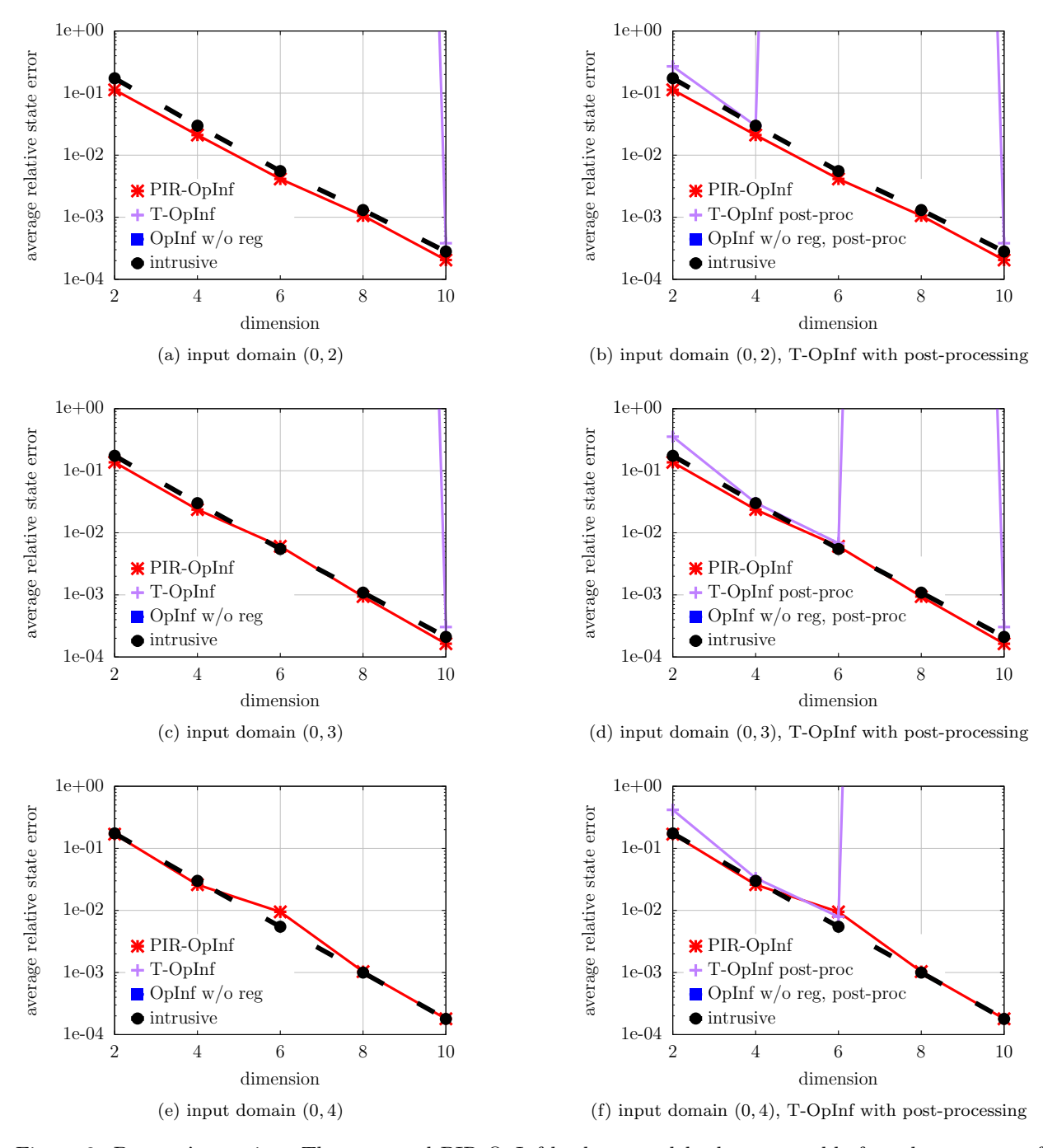
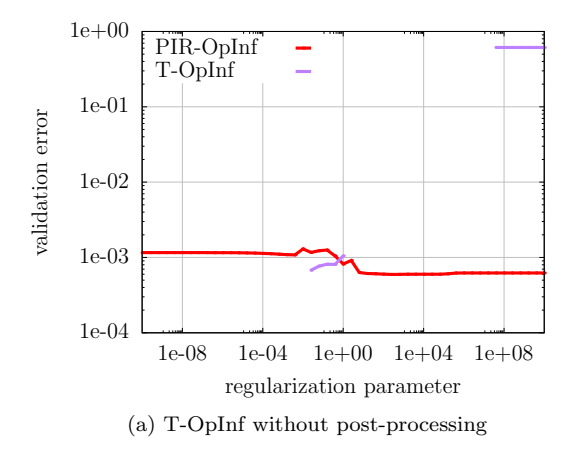
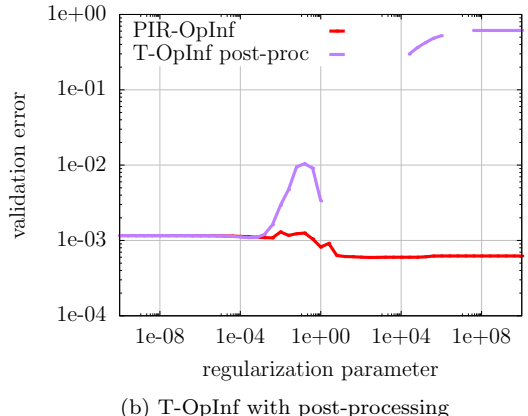


Figure 3: Burgers' equation: The proposed PIR-OpInf leads to models that are stable for a large range of inputs, which is in contrast to OpInf without regularization and OpInf with Tikhonov regularization (T-OpInf). The results also show that applying the same post-processing as for PIR-OpInf (cf. Section 3.4) to T-OpInf has little effect on the stability of the learned models, which indicates that indeed the proposed regularizer in PIR-OpInf is responsible for obtaining more stable models.





(b) T-OpInf with post-processing

Figure 4: Burgers' equation: The validation error (objective of (29)) of T-OpInf grows quickly with the regularization parameter, which means that the regularization has a negative effect on the model accuracy. In contrast, the validation error corresponding to the proposed PIR-OpInf is less sensitive to the regularization parameter, which means that large regularization parameters can be chosen—imposing a stronger stability bias—without deteriorating the model accuracy.

shows unstable behavior for many dimensions n. To separate the effect of the regularization from the effect of the post-processing (cf. Section 3.4), we apply the same post-processing as for PIR-OpInf to T-OpInf. The corresponding results in Figure 3b, Figure 3d, and Figure 3f show that post-processing helps to stabilize T-OpInf as well; however, as the range of the inputs increases, a similarly unstable behavior as in the case without post-processing is obtained. Thus, the results indicate that penalizing the quadratic term via the proposed regularizer is responsible for achieving stabler models, rather than the post processing or penalizing both the linear and the quadratic term together as in Tikhonov regularization, which is in agreement with the theoretical motivation outlined in Section 3.1.

Consider now Figure 4 that shows the validation error, i.e., the objective of (29), of the parameterselection procedure versus the regularization parameter for dimension n=8 for PIR-OpInf and T-OpInf. Independent of whether post-processing is applied to T-OpInf (Figure 4b) or not (Figure 4a), the error of T-OpInf grows quickly as the regularization parameter is increased. Thus, if a small regularization parameter is chosen, the validation error of T-OpInf is small but it also means that no regularization is induced. If instead the regularization parameter is large, then there might be a stability bias but at the same time it leads to a distinct increase of the model error. In contrast, the curves corresponding to PIR-OpInf show that the validation error is small for moderately sized regularization parameters, where a stability bias is induced without leading to a deterioration of the model accuracy.

Figure 5a shows the estimated stability radius (16) for various models. The results indicate that PIR-OpInf achieves a larger stability radius than the models obtained with T-OpInf and OpInf without regularization. At dimension n=2, the stability radius of PIR-OpInf is large because only large regularization parameters lead to stable behavior; see Figure 5b. The regularization parameter is chosen so large that the norm of the quadratic term is close to zero, which explains the high estimated stability radius.

Results for SPIR-OpInf 5.2.3

We now apply SPIR-OpInf to learn a symmetric and definite linear operator, which is in contrast to PIR-OpInf that does not impose any structure on the linear operator; see Figure 6a. Figure 7 shows the test error (34) corresponding to SPIR-OpInf. Stable behavior is obtained in all cases; however, a leveling off of the error as the dimension increases indicates that restricting to symmetric operators in this example is limiting the accuracy. Operator inference, independent of the used regularizer, is fitting operators to projected

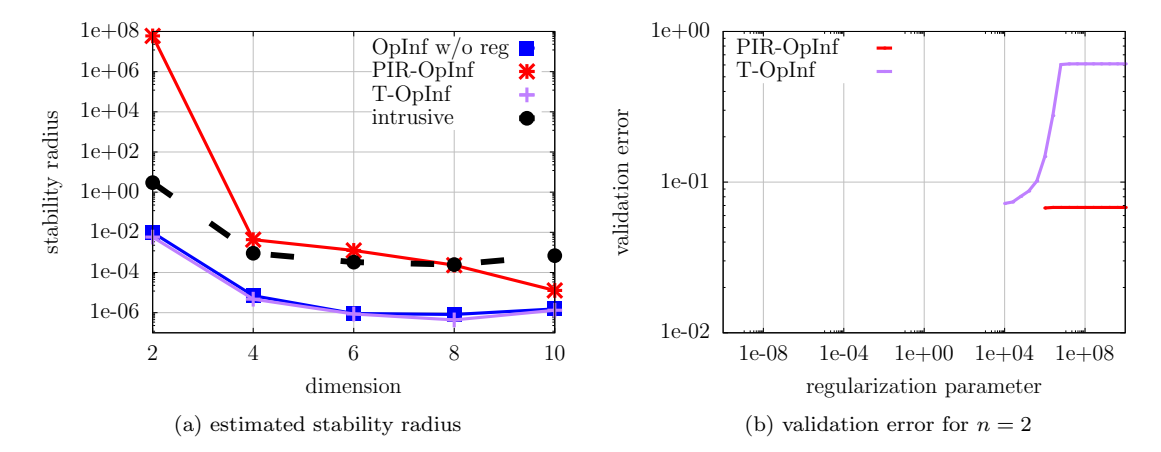


Figure 5: Burgers' equation: The models learned with the proposed PIR-OpInf have larger estimated stability radii than models obtained without regularization and with Tikhonov regularization (T-OpInf). The stability radius for n = 2 is high for PIR-OpInf models because only large regularization parameters $\lambda^* = 10^6$ lead to stable behavior (see (b)), which forces the norm of the quadratic term to be close to zero and thus increases the stability radius by a large amount. Notice that the PIR-OpInf model at n = 2 achieves a similar accuracy as intrusive model reduction; cf. Figure 3.

trajectories of the high-dimensional systems. Projected trajectories are different from reduced trajectories that are generated with the corresponding reduced model obtained with intrusive model reduction; see [48]. The difference between the projected and reduced trajectories is the closure error. This means that operator inference aims to find operators that well predict the projected trajectories, and the best operators (in the sense of the objective of operator inference) do not necessarily have the same structure as the intrusive operators. Thus, allowing operator inference to break structure can help in terms of accuracy, as can be seen by comparing Figure 3 with Figure 7. Additional constraints such as symmetry that are imposed by SPIR-OpInf on the linear operator mean that the optimization search space is smaller and thus SPIR-OpInf can lead to models that have a larger error than having no structure as in PIR-OpInf. However, breaking structure also means that predictions can become unphysical. Preventing such unphysical behavior is the motivation for structure preservation with SPIR-OpInf.

The estimated stability radii of the SPIR-OpInf models are compared to the stability radii of T-OpInf models in Figure 8a. For large dimensions n > 4, the estimated stability radii of the SPIR-OpInf models is larger than the stability radii of the T-OpInf models. For small dimensions $n \le 4$, the stability radii of SPIR-OpInf and T-OpInf models is large. This is reflected by the small regularization parameter selected by the proposed parameter selection procedure, which selects $\lambda \approx 3 \times 10^{-7}$ for n = 2.

5.3 Reaction-diffusion problem

Consider the parameterized reaction-diffusion equation

$$\frac{\partial}{\partial t}x(\boldsymbol{\xi},t;\boldsymbol{\mu}) = \Delta x(\boldsymbol{\xi},t;\boldsymbol{\mu}) + s(\boldsymbol{\xi})u(t) + g(x(\boldsymbol{\xi},t;\boldsymbol{\mu})), \qquad (35)$$

with the spatial coordinate $\boldsymbol{\xi} = [\xi_1 \ \xi_2]^T \in [0,1]^2$. We impose homogeneous Neumann boundary conditions. The parameter domain is $\mathcal{D} = [1,1.5]$ and end time is T = 20. The source is $s(\boldsymbol{\xi}) = 10^{-1} \sin(2\pi \xi_1) \sin(2\pi \xi_2)$. The nonlinear term is

$$g(x(\xi,t;\mu)) = -(a\sin(\mu) + 2)\exp(-\mu^2 b) \left(1 + (\mu c)x + \frac{(\mu c)^2}{2!}x^2\right)$$

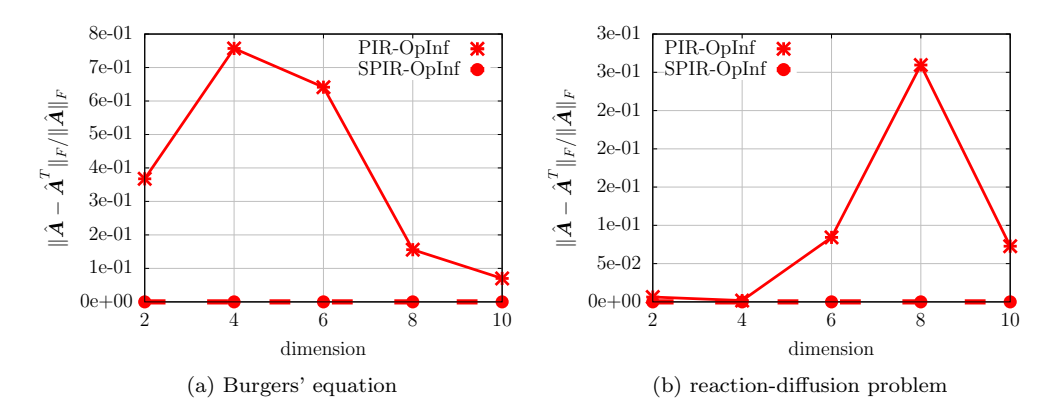


Figure 6: Structure such as symmetry in the matrix \hat{A} can be imposed via SPIR-OpInf.

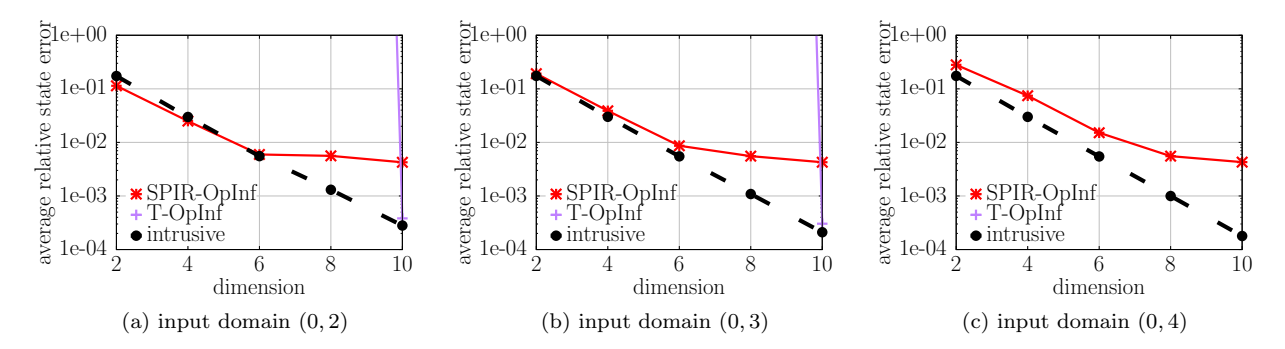


Figure 7: Burgers' equation: Imposing symmetry and definiteness onto the linear operator with the proposed SPIR-OpInf (25) leads to stable models in this experiment; however, the additional constraints lead to a lower accuracy than PIR-OpInf that include the proposed regularizer but no constraints on the linear operator (cf. Figure 3).

which is the second-order Taylor approximation of the source term used in [48], with a = 0.1, b = 2.7 and c = 1.8. We discretize in space with a mesh width of h = 1/12 and finite difference and in time with explicit Euler with time-step size $\delta t = 10^{-2}$. The dimension of the high-dimensional model is N = 144.

The training parameter set contains the M=10 equidistant points in the parameter domain \mathcal{D} . To construct the reduced space, we take a single $M_b=1$ input trajectory for each training parameter, where the inputs are sampled uniformly in [0,1]. The initial condition is zero. The corresponding trajectories $\mathbf{X}_1^{\mathrm{b}}(\mu_1),\ldots,\mathbf{X}_1^{\mathrm{b}}(\mu_M)$ are used to construct a POD basis. For each of the M training parameters, we sample $M_t=10$ input trajectories with entries uniformly in [0,1]. The regularization parameters are selected via our selection procedure described in Section 4.2 by sweeping over the 51 logarithmically equidistant points in $[10^{-10},10^{10}]$. We test models for $M_{\mathrm{test}}=7$ test parameters that are equidistantly distributed in the parameter domain \mathcal{D} . For every test parameter $\mu_1^{\mathrm{test}},\ldots,\mu_{M_{\mathrm{test}}}^{\mathrm{test}}$, we generate a single input trajectory $\mathbf{U}^{\mathrm{test}}$, whose entries randomly selected via a uniform distribution in [0,1], and initial condition $\mathbf{x}_0^{\mathrm{test}}=\mathbf{0}$. The test error is then

$$e_{\text{test}} = \sum_{i=1}^{M_{\text{test}}} \frac{\|\boldsymbol{V}\bar{\boldsymbol{X}}^{\text{test}}(\boldsymbol{\mu}_{i}^{\text{test}}) - \boldsymbol{X}^{\text{test}}(\boldsymbol{\mu}_{i}^{\text{test}})\|_{F}}{\|\boldsymbol{X}^{\text{test}}(\boldsymbol{\mu}_{i}^{\text{test}})\|_{F}},$$
(36)

where $\bar{X}^{\text{test}}(\mu_i^{\text{test}})$ is the predicted trajectory at parameter μ_i^{test} by either the PIR-OpInf, T-OpInf, OpInf without regularization, or intrusive model reduction.

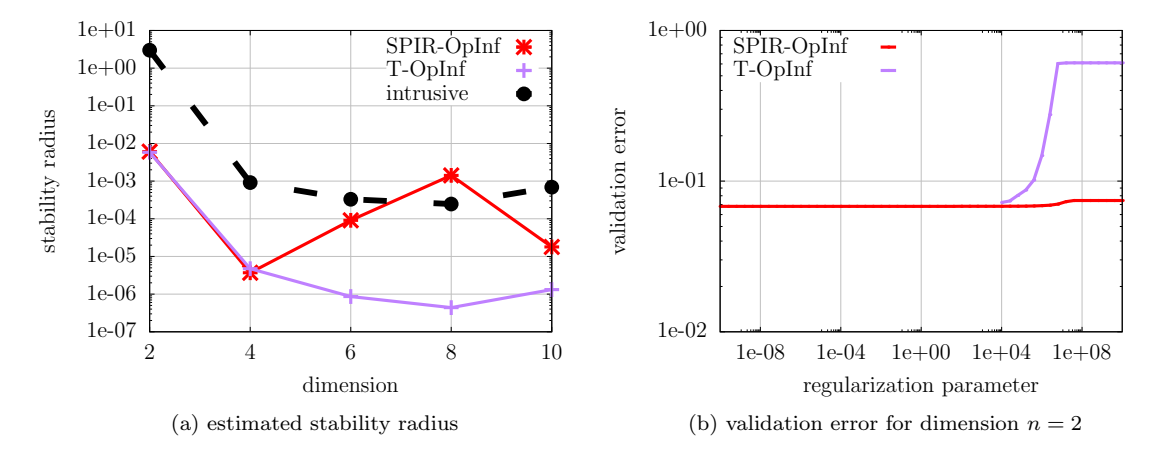


Figure 8: Burgers' equation: Models learned with SPIR-OpInf have a larger estimated stability radius than models learned with Tikhonov regularization for dimensions n > 4 in this example. The stability radius of the SPIR-OpInf model is similar to the stability radius of the T-OpInf model for n = 2 because a small regularization parameter is chosen as shown in plot (b).

Figure 9a shows the test error (36). The results indicate that OpInf without any regularization becomes unstable quickly. In contrast, T-OpInf and PIR-OpInf provide stable approximations. However, whereas the Tikhonov regularization in T-OpInf leads to a loss of accuracy at higher dimensions, the proposed physics-informed regularizer used by PIR-OpInf achieves errors that are comparable to intrusive model reduction. This is in agreement with the estimated stability radius shown in Figure 9b, where PIR-OpInf achieves an orders of magnitude larger stability radius at higher dimensions n than T-OpInf and OpInf without regularization. Similar results are obtained with SPIR-OpInf, where symmetry and definiteness are imposed, as shown in Figure 10; see also Figure 6b.

5.4 Phase separation described by Allen-Cahn equation

Consider the cubic nonlinear Allen-Cahn model that is used, for example, for describing phase transitions:

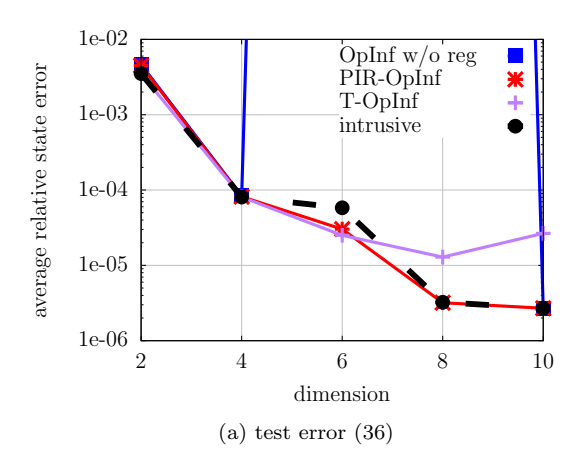
$$\frac{\partial}{\partial t}x(\omega,t) = \frac{\partial^2}{\partial^2\omega}x(\omega,t) - x(\omega,t)^3 + u(t), \qquad (37)$$

with spatial coordinate $\omega \in (0,1)$ and time $t \in [0,0.1]$. The boundary conditions are

$$x(0,t) = u(t), \quad \frac{\partial x}{\partial t}(1,t) = 0,$$

with input $u(t): [0,1] \to \mathbb{R}$. The equation is discretized in space with finite differences on an equidistant grid in [0,1] with N=128 grid points. Time is discretized with the explicit Euler method with time-step size $\delta t = 10^{-5}$.

To construct the basis of a reduced space, we take a single $M_b = 1$ input trajectory, where the inputs are sampled uniformly in [0, 10]. The initial condition is zero. The corresponding trajectory X^b is used to construct a POD basis. For training the model, we use $M_t = 10$ input trajectories, with entries uniformly sampled in [0, 10]. The regularization parameters are selected via our selection procedure described in Section 4.3 by sweeping over the 51 logarithmically equidistant points in $[10^{-10}, 10^{10}]$, where the validation data consists of the training trajectories and the trajectory obtained with input $U^{\text{val}} = 10(\sin(\pi t) + 1), t \in [0, 0.1]$. We test models for the test input trajectory $U^{\text{test}} = 25(\sin(\pi t) + 1), t \in [0, 0.1]$, which is motivated by the work [64]. The reduced model is simulated for the test input and the generated state trajectory is compared against the corresponding full model trajectory.



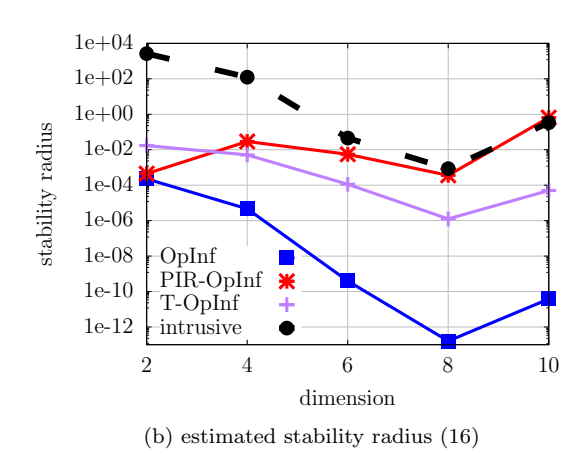
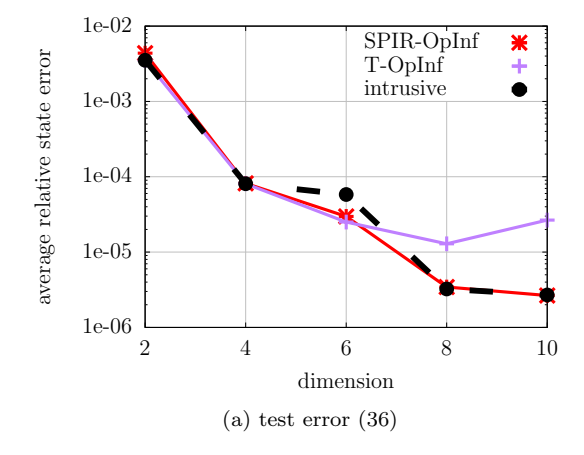


Figure 9: Reaction-diffusion problem: The PIR-OpInf model shows stable behavior in this experiment. In contrast to Tikhonov regularization (T-OpInf), the PIR-OpInf model achieves an accuracy close to intrusive model reduction even for larger n>6 dimensions. The estimated stability radius of the PIR-OpInf model is orders of magnitude higher than the stability radius of the T-OpInf model in this experiment.



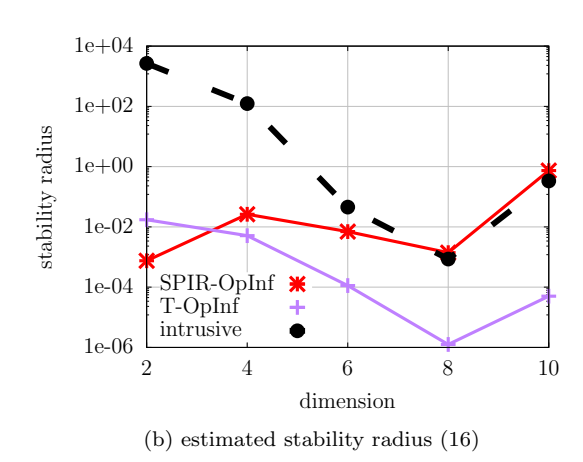
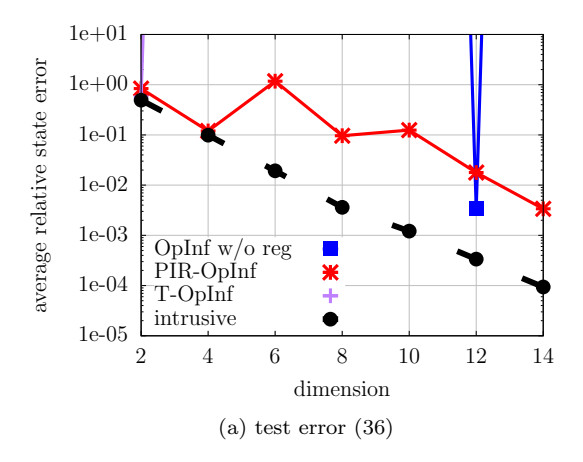


Figure 10: Reaction-diffusion problem: Constraining the linear inferred operator to be symmetric and definite with SPIR-OpInf leads to models with comparable accuracy and stability radius as PIR-OpInf in this example.



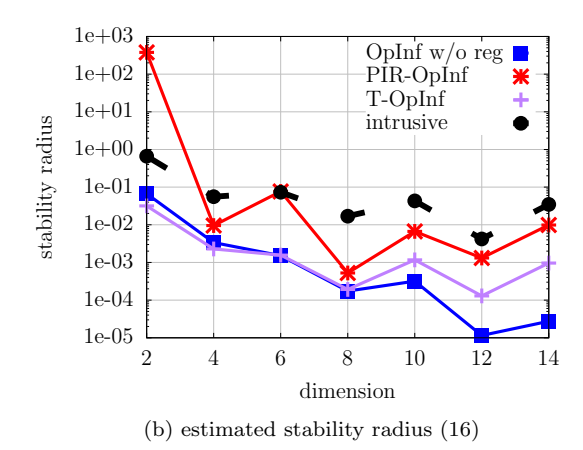


Figure 11: Allen-Cahn model: The PIR-OpInf model shows stable behavior in this experiment, whereas Tikhonov regularization is unstable for all dimensions except 2. The estimated stability radius of the PIR-OpInf model is higher than the stability radius of the T-OpInf model.

Figure 11a shows the test error (36). The results indicate that OpInf without any regularization and T-OpInf are unstable for most dimensions, whereas PIR-OpInf provides a stable solution for all dimensions. Our parameter selection scheme for PIR-OpInf selects the regularization parameters $\lambda^* = 10^{12}, 1.58 \times 10^9, 1.58 \times 10^{10}, 3.98 \times 10^5, 3.98 \times 10^6, 3.98 \times 10^6, 2.51 \times 10^5$ for dimensions n = 2, 4, 6, 8, 10, 12, 14, respectively. The selected regularization parameters show that a strong regularization is necessary in this example. At the same time, the large values of the selected regularization parameter results in PIR-OpInf to have a higher test error compared to the intrusive model. As seen in Figure 11b, PIR-OpInf achieves a larger stability radius at all dimensions n than both T-OpInf and OpInf without regularization.

5.5 FitzHugh-Nagumo equation

Consider the FitzHugh-Nagumo equation with quadratic and cubic nonlinear terms:

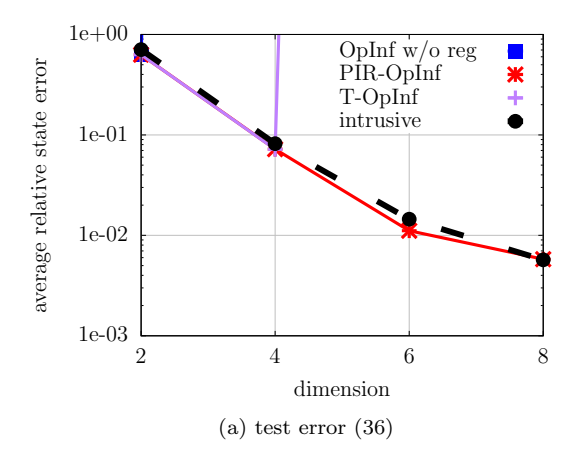
$$\epsilon \frac{\partial v}{\partial t}(\omega, t) = \epsilon^2 \nabla^2 v(\omega, t) - v(\omega, t)(v(\omega, t) - R)(1 - v(\omega, t)) - w(\omega, t) + c,
\frac{\partial w}{\partial t}(\omega, t) = bv(\omega, t) - \gamma w(\omega, t) + c$$
(38)

with spatial coordinate $\omega \in (0,1)$, time $t \in [0,8]$. The equation is discretized in space with finite differences on an equidistant grid with N=128 grid points for both $v(\omega,t)$ and $w(\omega,t)$. In time, we use as discretization the the semi-implicit Euler method with time-step size $\delta t=10^{-3}$. The parameter values for FitzHugh-Nagumo equation are $\epsilon=0.05, R=1, c=0.05, b=5$ and $\gamma=20$. Parameter values are not varied when learning the model but different initial conditions (see below) and different inputs are used that enter via the boundary conditions:

$$v_{\omega}(0,t) = -i_0 t^3 \exp(-i_1 t), \ v_{\omega}(1,t) = 0, \qquad t \ge 0,$$

where i_0 is uniformly sampled in [49500, 50500], and i_1 is uniformly sampled in [14, 16], when generating data trajectories for basis generation and training, while constant values $i_0 = 50000, i_1 = 15$ is used for testing.

To construct the reduced space, we take $M_b = 5$ input trajectories, and zero initial condition. The corresponding trajectory X^b is used to construct a POD basis. For training the model, we use $M_t = 10$ input trajectories, and initial conditions with entries uniformly sampled in [-0.1, 0.1]. The regularization parameters are selected via our selection procedure described in Section 4.3 by sweeping over the 51 logarithmically equidistant points in $[10^{-10}, 10^{10}]$. We test models for the test input trajectory given above and zero initial



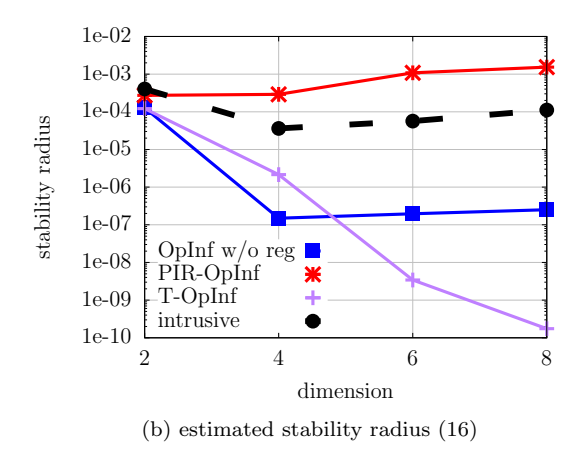


Figure 12: FitzHugh-Nagumo: PIR-OpInf learns stable models, while OpInf without regularization gives unstable models for dimensions > 2, and T-OpInf is unstable for dimensions > 4. Of all the inferred models, PIR-OpInf learns the reduced model with the largest estimated stability radius $(\hat{\rho})$, and for dimensions 6 and 8, $\hat{\rho}$ for PIR-OpInf is considerably larger compared to the models learned via T-OpInf.

condition, which is different from the training initial conditions. The reduced model is simulated for the test input and the generated state trajectory is compared against the corresponding full model trajectory. Figure 12a shows the test error (36). The results indicate that OpInf without any regularization is unstable for all dimensions > 2. For PIR-OpInf, the solution is stable for all dimensions, and the test error is close to the error of the intrusive model. T-OpInf is unstable for dimensions > 4. Figure 12b shows that among all of the inferred models, PIR-OpInf gives the model with the largest stability radius. For dimensions 6 and 8, our parameter selection scheme selects regularization parameters $\lambda^* = 10^2$ and $\lambda^* = 10$ for PIR-OpInf and $\lambda^* = 10^8$ and $\lambda^* = 1.58 \times 10^9$ for T-OpInf. T-OpInf regularizes all parameters with a large regularization parameter, which results in a model with a small $\|\hat{A}\|_F$. As the equation (15) computes the Lyapunov matrix P, a model with a small $\|\hat{A}\|_F$, leads to a model with a large $\|P\|_F$. A large $\|P\|_F$ results in a smaller $\hat{\rho}$ (20), and consequently, a less stable model, which is in agreement with the numerical results shown in Figure 12b.

6 Conclusions

Learning models from data is an ever more important task in science and engineering. It is increasingly recognized that physical insights need to be incorporated together with data to learn truly predictive models [1, 2]. In this spirit, we proposed a regularizer that explicitly leverages the quadratic-cubic model form, which in turn is imposed by the underlying physics, to penalize unstable models learned with operator inference. We also showed that additional physical insights in the form of structure of the linear dynamics can be imposed on the operator-inference models via constraints. In our experiments, operator inference with the proposed physics-informed regularizer and structure preservation outperforms operator inference without regularization and operator inference with Tikhonov regularization in terms of stability and accuracy. Thus, our results provide evidence of the importance of combining physical insights and data for deriving predictive models in science and engineering. There are many avenues for future research. We highlight one immediate research direction, which is combining the physics-informed regularizer proposed in this work with lifting maps that lift cubic, high-order polynomial, and more generally nonlinear systems into quadratic systems, see [78, 64, 7]. There typically are multiple lifting maps and we expect that the stability properties depend on the specific map that is used. It thus would be interesting to determine which maps are favorable over other maps in terms of stability.

Acknowledgements

The first and third author acknowledge partially supported by US Department of Energy, Office of Advanced Scientific Computing Research, Applied Mathematics Program (Program Manager Dr. Steven Lee), DOE Award DESC0019334, and by the National Science Foundation under Grant No. 1901091 and under Grant No. 1761068. The second author acknowledges support by the Korean Ministry of Trade, Industry and Energy (MOTIE) and the Korea Institute for Advancement of Technology (KIAT) through the International Cooperative R&D program (No. P0019804, Digital twin based intelligent unmanned facility inspection solutions).

References

- [1] P. V. Coveney, E. R. Dougherty, R. R. Highfield, Big data need big theory too, Philosophical Transactions of the Royal Society A: Mathematical, Physical and Engineering Sciences 374 (2080) (2016) 20160153.
- [2] K. E. Willcox, O. Ghattas, P. Heimbach, The imperative of physics-based modeling and inverse theory in computational science, Nature Computational Science 1 (3) (2021) 166–168.
- [3] S. L. Brunton, J. L. Proctor, J. N. Kutz, Discovering governing equations from data by sparse identification of nonlinear dynamical systems, Proceedings of the National Academy of Sciences 113 (15) (2016) 3932–3937.
- [4] R. Swischuk, L. Mainini, B. Peherstorfer, K. Willcox, Projection-based model reduction: Formulations for physics-based machine learning, Computers & Fluids 179 (2019) 704–717.
- [5] M. Raissi, P. Perdikaris, G. E. Karniadakis, Physics-informed neural networks: A deep learning framework for solving forward and inverse problems involving nonlinear partial differential equations, Journal of Computational Physics 378 (2019) 686–707.
- [6] K. Duraisamy, G. Iaccarino, H. Xiao, Turbulence modeling in the age of data, Annual Review of Fluid Mechanics 51 (1) (2019) 357–377.
- [7] E. Qian, B. Kramer, B. Peherstorfer, K. Willcox, Lift & learn: Physics-informed machine learning for large-scale nonlinear dynamical systems, Physica D: Nonlinear Phenomena 406 (2020) 132401.
- [8] L. Ljung, System identification, Prentice Hall, 1987.
- [9] A. C. Antoulas, B. D. O. Anderson, On the scalar rational interpolation problem, IMA Journal of Mathematical Control and Information 3 (2-3) (1986) 61–88.
- [10] A. J. Mayo, A. C. Antoulas, A framework for the solution of the generalized realization problem, Linear algebra and its applications 425 (2-3) (2007) 634–662.
- [11] A. C. Antoulas, C. A. Beattie, S. Gugercin, Interpolatory Methods for Model Reduction, SIAM, 2021.
- [12] A. C. Ionita, A. C. Antoulas, Data-driven parametrized model reduction in the Loewner framework, SIAM Journal on Scientific Computing 36 (3) (2014) A984–A1007.
- [13] I. V. Gosea, M. Petreczky, A. C. Antoulas, Data-driven model order reduction of linear switched systems in the Loewner framework, SIAM Journal on Scientific Computing 40 (2) (2018) B572–B610.
- [14] P. Schulze, B. Unger, C. Beattie, S. Gugercin, Data-driven structured realization, Linear Algebra and its Applications 537 (2018) 250–286.
- [15] P. Schulze, B. Unger, Data-driven interpolation of dynamical systems with delay, Systems & Control Letters 97 (2016) 125–131.

- [16] A. C. Antoulas, I. V. Gosea, A. C. Ionita, Model reduction of bilinear systems in the Loewner framework, SIAM Journal on Scientific Computing 38 (5) (2016) B889–B916.
- [17] I. V. Gosea, D. S. Karachalios, A. C. Antoulas, Learning reduced-order models of quadratic dynamical systems from input-output data, in: 2021 European Control Conference (ECC), 2021, pp. 1426–1431.
- [18] I. V. Gosea, A. C. Antoulas, Data-driven model order reduction of quadratic-bilinear systems, Numerical Linear Algebra with Applications 25 (6) (2018) e2200.
- [19] P. Benner, P. Goyal, Interpolation-based model order reduction for polynomial systems, SIAM Journal on Scientific Computing 43 (1) (2021) A84–A108.
- [20] I. V. Gosea, M. Petreczky, A. C. Antoulas, Reduced-order modeling of LPV systems in the Loewner framework, in: 2021 60th IEEE Conference on Decision and Control (CDC), 2021, pp. 3299–3305.
- [21] B. Peherstorfer, S. Gugercin, K. Willcox, Data-driven reduced model construction with time-domain Loewner models, SIAM Journal on Scientific Computing 39 (5) (2017) A2152–A2178.
- [22] D. S. Karachalios, I. V. Gosea, A. C. Antoulas, On Bilinear Time-Domain Identification and Reduction in the Loewner Framework, Springer International Publishing, Cham, 2021, pp. 3–30.
- [23] S. Lefteriu, A. C. Ionita, A. C. Antoulas, Modeling systems based on noisy frequency and time domain measurements, in: J. C. Willems, S. Hara, Y. Ohta, H. Fujioka (Eds.), Perspectives in Mathematical System Theory, Control, and Signal Processing: A Festschrift in Honor of Yutaka Yamamoto on the Occasion of his 60th Birthday, Springer Berlin Heidelberg, Berlin, Heidelberg, 2010, pp. 365–378.
- [24] M. Embree, A. C. Ionita, Pseudospectra of Loewner matrix pencils, in: C. Beattie, P. Benner, M. Embree, S. Gugercin, S. Lefteriu (Eds.), Realization and Model Reduction of Dynamical Systems: A Festschrift in Honor of the 70th Birthday of Thanos Antoulas, Springer International Publishing, Cham, 2022, pp. 59–78.
- [25] Z. Drmač, B. Peherstorfer, Learning low-dimensional dynamical-system models from noisy frequency-response data with Loewner rational interpolation, in: C. Beattie, P. Benner, M. Embree, S. Gugercin, S. Lefteriu (Eds.), Realization and Model Reduction of Dynamical Systems: A Festschrift in Honor of the 70th Birthday of Thanos Antoulas, Springer International Publishing, Cham, 2022, pp. 39–57.
- [26] P. J. Schmid, Dynamic mode decomposition of numerical and experimental data, Journal of fluid mechanics 656 (2010) 5–28.
- [27] C. W. Rowley, I. Mezic, S. Bagheri, P. Schlatter, D. S. Henningson, Spectral analysis of nonlinear flows, Journal of Fluid Mechanics 641 (2009) 115–127.
- [28] J. H. Tu, C. W. Rowley, D. M. Luchtenburg, S. L. Brunton, J. N. Kutz, On dynamic mode decomposition: Theory and applications, Journal of Computational Dynamics 1 (2) (2014) 391–421.
- [29] J. N. Kutz, S. L. Brunton, B. W. Brunton, J. L. Proctor, Dynamic mode decomposition: data-driven modeling of complex systems, SIAM, 2016.
- [30] I. Mezić, Spectral properties of dynamical systems, model reduction and decompositions, Nonlinear Dynamics 41 (1-3) (2005) 309–325.
- [31] M. O. Williams, I. G. Kevrekidis, C. W. Rowley, A data-driven approximation of the Koopman operator: Extending dynamic mode decomposition, Journal of Nonlinear Science 25 (6) (2015) 1307–1346.
- [32] S. L. Brunton, B. W. Brunton, J. L. Proctor, J. N. Kutz, Koopman invariant subspaces and finite linear representations of nonlinear dynamical systems for control, PloS one 11 (2) (2016) e0150171.

- [33] H. Schaeffer, R. Caflisch, C. D. Hauck, S. Osher, Sparse dynamics for partial differential equations, Proceedings of the National Academy of Sciences 110 (17) (2013) 6634–6639.
- [34] H. Schaeffer, Learning partial differential equations via data discovery and sparse optimization, Proceedings of the Royal Society A: Mathematical, Physical and Engineering Sciences 473 (2197) (2017) 20160446.
- [35] G. Tran, R. Ward, Exact recovery of chaotic systems from highly corrupted data, Multiscale Modeling & Simulation 15 (3) (2017) 1108–1129.
- [36] A. A. Kaptanoglu, J. L. Callaham, A. Aravkin, C. J. Hansen, S. L. Brunton, Promoting global stability in data-driven models of quadratic nonlinear dynamics, Phys. Rev. Fluids 6 (2021) 094401.
- [37] S. L. Brunton, J. N. Kutz, Data-driven science and engineering. Machine learning, dynamical systems, and control., Cambridge University Press, 2022.
- [38] N. B. Erichson, M. Muehlebach, M. Mahoney, Physics-informed autoencoders for Lyapunov-stable fluid flow prediction, in: Machine Learning and the Physical Sciences Workshop, Conference on Neural Information Processing Systems, 2019, pp. 1–14.
- [39] R. E. Morrison, T. A. Oliver, R. D. Moser, Representing model inadequacy: A stochastic operator approach, SIAM/ASA Journal on Uncertainty Quantification 6 (2) (2018) 457–496.
- [40] B. D. Tracey, K. Duraisamy, J. J. Alonso, A machine learning strategy to assist turbulence model development, in: 53rd AIAA Aerospace Sciences Meeting, AIAA, 2015, pp. 1–15.
- [41] R. Maulik, O. San, A neural network approach for the blind deconvolution of turbulent flows, Journal of Fluid Mechanics 831 (2017) 151–181.
- [42] R. Maulik, O. San, A. Rasheed, P. Vedula, Subgrid modelling for two-dimensional turbulence using neural networks, Journal of Fluid Mechanics 858 (2019) 122–144.
- [43] M. Benosman, J. Borggaard, O. San, B. Kramer, Learning-based robust stabilization for reduced-order models of 2d and 3d Boussinesq equations, Applied Mathematical Modelling 49 (2017) 162–181.
- [44] X. Xie, M. Mohebujjaman, L. G. Rebholz, T. Iliescu, Data-driven filtered reduced order modeling of fluid flows, SIAM Journal on Scientific Computing 40 (3) (2018) B834–B857.
- [45] S. Pan, K. Duraisamy, Data-driven discovery of closure models, SIAM Journal on Applied Dynamical Systems 17 (4) (2018) 2381–2413.
- [46] M. Benosman, J. Borggaard, B. Kramer, Robust POD model stabilization for the 3d Boussinesq equations based on Lyapunov theory and extremum seeking, in: American Control Conference (ACC), IEEE, 2017, pp. 1827–1832.
- [47] B. Peherstorfer, K. Willcox, Data-driven operator inference for nonintrusive projection-based model reduction, Computer Methods in Applied Mechanics and Engineering 306 (2016) 196–215.
- [48] B. Peherstorfer, Sampling low-dimensional Markovian dynamics for pre-asymptotically recovering reduced models from data with operator inference, SIAM Journal on Scientific Computing 42 (2020) A3489–A3515.
- [49] W. I. T. Uy, B. Peherstorfer, Probabilistic error estimation for non-intrusive reduced models learned from data of systems governed by linear parabolic partial differential equations, ESAIM: M2AN 55 (3) (2021) 735–761.
- [50] W. I. T. Uy, B. Peherstorfer, Operator inference of non-Markovian terms for learning reduced models from partially observed state trajectories, Journal of Scientific Computing 88 (3) (2021) 91.

- [51] E. Qian, B. Kramer, A. Marques, K. Willcox, Transform & learn: A data-driven approach to nonlinear model reduction, in: AIAA Aviation 2019 Forum, AIAA, 2019, pp. 1–11.
- [52] P. Benner, P. Goyal, B. Kramer, B. Peherstorfer, K. Willcox, Operator inference for non-intrusive model reduction of systems with non-polynomial nonlinear terms, Computer Methods in Applied Mechanics and Engineering 372 (2020) 113433.
- [53] P. Khodabakhshi, K. E. Willcox, Non-intrusive data-driven model reduction for differential-algebraic equations derived from lifting transformations, Computer Methods in Applied Mechanics and Engineering 389 (2022) 114296.
- [54] H. Sharma, Z. Wang, B. Kramer, Hamiltonian operator inference: Physics-preserving learning of reduced-order models for Hamiltonian systems, Physica D: Nonlinear Phenomena 431 (2022) 133122.
- [55] W. I. T. Uy, Y. Wang, Y. Wen, B. Peherstorfer, Active operator inference for learning low-dimensional dynamical-system models from noisy data, arXiv 2107.09256.
- [56] H. Sharma, B. Kramer, Preserving Lagrangian structure in data-driven reduced-order modeling of large-scale mechanical systems, arXiv preprint arXiv:2203.06361.
- [57] P. Benner, P. Goyal, J. Heiland, I. P. Duff, Operator inference and physics-informed learning of low-dimensional models for incompressible flows, Electronic Transactions on Numerical Analysis 56 (2022) 28–51.
- [58] R. Swischuk, B. Kramer, C. Huang, K. Willcox, Learning physics-based reduced-order models for a single-injector combustion process, AIAA Journal 58 (6) (2020) 2658–2672.
- [59] S. A. McQuarrie, C. Huang, K. Willcox, Data-driven reduced-order models via regularised operator inference for a single-injector combustion process, Journal of the Royal Society of New Zealand 51 (2) (2021) 194–211.
- [60] E. Qian, A scientific machine learning approach to learning reduced models for nonlinear partial differential equations, Ph.D. thesis, Massachusetts Institute of Technology (2021).
- [61] A. Tesi, F. Villoresi, R. Genesio, On stability domain estimation via a quadratic Lyapunov function: convexity and optimality properties for polynomial systems, in: Proceedings of 1994 33rd IEEE Conference on Decision and Control, Vol. 2, 1994, pp. 1907–1912.
- [62] G. Chesi, Estimating the domain of attraction via union of continuous families of Lyapunov estimates, Systems & Control Letters 56 (4) (2007) 326–333.
- [63] B. Kramer, Stability domains for quadratic-bilinear reduced-order models, SIAM Journal on Applied Dynamical Systems 20 (2) (2021) 981–996.
- [64] P. Benner, T. Breiten, Two-sided projection methods for nonlinear model order reduction, SIAM Journal on Scientific Computing 37 (2) (2015) B239–B260.
- [65] R. Genesio, A. Tesi, Stability analysis of quadratic systems, IFAC Proceedings Volumes 22 (3) (1989) 195–199.
- [66] A. C. Antoulas, Approximation of large-scale dynamical systems, SIAM, 2005.
- [67] G. Rozza, D. B. P. Huynh, A. T. Patera, Reduced basis approximation and a posteriori error estimation for affinely parametrized elliptic coercive partial differential equations, Archives of Computational Methods in Engineering 15 (3) (2007) 1.
- [68] A. C. Antoulas, C. A. Beattie, S. Gugercin, Interpolatory model reduction of large-scale dynamical systems, in: Efficient modeling and control of large-scale systems, Springer, 2010, pp. 3–58.

- [69] P. Benner, S. Gugercin, K. Willcox, A survey of projection-based model reduction methods for parametric dynamical systems, SIAM review 57 (4) (2015) 483–531.
- [70] Z. Lin, Riemannian geometry of symmetric positive definite matrices via Cholesky decomposition, SIAM Journal on Matrix Analysis and Applications 40 (4) (2019) 1353–1370.
- [71] N. J. Higham, Computing a nearest symmetric positive semidefinite matrix, Linear Algebra and its Applications 103 (1988) 103–118.
- [72] I. Kalashnikova, B. van Bloemen Waanders, S. Arunajatesan, M. Barone, Stabilization of projection-based reduced order models for linear time-invariant systems via optimization-based eigenvalue reassignment, Computer Methods in Applied Mechanics and Engineering 272 (2014) 251–270.
- [73] I. V. Gosea, A. C. Antoulas, Stability preserving post-processing methods applied in the Loewner framework, in: 2016 IEEE 20th Workshop on Signal and Power Integrity (SPI), 2016, pp. 1–4.
- [74] M. Köhler, On the closest stable descriptor system in the respective spaces RH_2 and RH_{∞} , Linear Algebra and its Applications 443 (2014) 34–49.
- [75] S. Boyd, L. Vandenberghe, Convex Optimization, Cambridge Press, 2009.
- [76] J. Degroote, J. Vierendeels, K. Willcox, Interpolation among reduced-order matrices to obtain parameterized models for design, optimization and probabilistic analysis, International Journal for Numerical Methods in Fluids 63 (2) (2010) 207–230.
- [77] D. Amsallem, C. Farhat, Interpolation method for adapting reduced-order models and application to aeroelasticity, AIAA journal 46 (7) (2008) 1803–1813.
- [78] C. Gu, Qlmor: A projection-based nonlinear model order reduction approach using quadratic-linear representation of nonlinear systems, IEEE Transactions on Computer-Aided Design of Integrated Circuits and Systems 30 (9) (2011) 1307–1320.